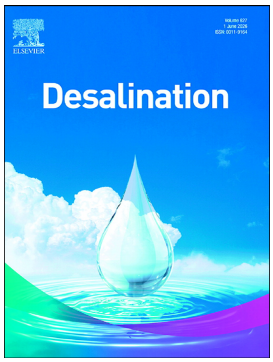
Journal Pre-proof



Tuning interfacial polymerization with aminated lignin for highly selective Li+/Mg2+ separation: Mechanistic insights from thermodynamic modeling and molecular dynamics simulations

Elham Jashni, Amirhossein Taghipour, Behzad Ahvazi, Filipe Hobi Bordon Sosa, André Nogueira, Aria Khalili, Aman Ullah, Jae-Young Cho, Mohtada Sadrzadeh

PII: S0011-9164(26)00948-3

DOI: https://doi.org/10.1016/j.desal.2026.120792

Reference: DES 120792

To appear in: *Desalination*

Received date: 14 June 2026

Revised date: 5 September 2026

Accepted date: 10 September 2026

Please cite this article as: E. Jashni, A. Taghipour, B. Ahvazi, et al., Tuning interfacial polymerization with aminated lignin for highly selective Li+/Mg2+ separation: Mechanistic insights from thermodynamic modeling and molecular dynamics simulations, *Desalination* (2026), https://doi.org/10.1016/j.desal.2026.120792

This is a PDF of an article that has undergone enhancements after acceptance, such as the addition of a cover page and metadata, and formatting for readability. This version will undergo additional copyediting, typesetting and review before it is published in its final form. As such, this version is no longer the Accepted Manuscript, but it is not yet the definitive Version of Record; we are providing this early version to give early visibility of the article. Please note that Elsevier's sharing policy for the Published Journal Article applies to this version, see: https://www.elsevier.com/about/policies-and-standards/sharing#4-published-journal-article. Please also note that, during the production process, errors may be discovered which could affect the content, and all legal disclaimers that apply to the journal pertain.

© 2026 Published by Elsevier B.V.

Tuning Interfacial Polymerization with Aminated Lignin for Highly Selective Li^+/Mg^{2+} Separation: Mechanistic Insights from Thermodynamic Modeling and Molecular Dynamics Simulations

Elham Jashni[1,2], Amirhossein Taghipour[1], Behzad Ahvazi[1,3], Filipe Hobi Bordon Sosa[4], André Nogueira[4], Aria Khalili[1,2], Aman Ullah[3], Jae-Young Cho[2], Mohtada Sadrzadeh[1*]

[1] Department of Mechanical Engineering, 10-241 Donadeo Innovation Center for Engineering, Advanced Water Research Lab (AWRL), University of Alberta, Edmonton, AB, Canada T6G 1H9

[2] Nanotechnology Research Center, National Research Council Canada, 11421 Saskatchewan Drive, Edmonton, AB, Canada, T6G 2M9

[3] Department of Agricultural, Food and Nutritional Science, Lipids/Materials Chemistry Group (LMCG), 360C South Academic Building, University of Alberta, Edmonton, AB, Canada T6G 2P5

[4] CICECO-Aveiro Institute of Materials, Department of Chemistry, University of Aveiro, 3810-193 Aveiro, Portugal.

Corresponding Author: Mohtada Sadrzadeh (sadrzade@ualberta.ca)

Journal Pre-proof

Abstract

Global efforts toward carbon neutrality have intensified the demand for efficient and sustainable Li^+ extraction from salt-lake brines. In this study, nanofiltration (NF) membranes with ultra-high Li^+/Mg^{2+} selectivity were fabricated via interfacial polymerization using aminated lignin (AL) as an additive in the piperazine (PIP) aqueous phase and trimesoyl chloride (TMC) in the organic phase. Conductor-like screening model for real solvents (COSMO-RS) calculations and molecular dynamics (MD) simulations indicated that AL acts as both a thermodynamic stabilizer and a kinetic modulator of PIP, suppressing its interfacial transport and redistributing monomer concentration near the reaction zone. This interfacial regulation alters polymerization kinetics, yielding a thinner and more structurally tailored polyamide selective layer. Zeta potential measurements revealed a reduction in membrane negativity after AL incorporation, consistent with enhanced Li^+/Mg^{2+} selectivity. In a 2000 ppm salt solution with a Li^+/Mg^{2+} ratio of 1:20, the optimized membrane (M-0.25 containing 0.25 wt% AL) achieved a Li^+/Mg^{2+} selectivity of 51.2, representing a 7.4-fold improvement over the unmodified membrane without compromising water flux. These findings demonstrate the potential of AL as a bio-based reactive additive for enhancing Li^+/Mg^{2+} selectivity in NF membranes, offering a promising strategy for lithium extraction from salt-lake brines.

Keywords: Li^+/Mg^{2+} separation; Lithium-selective nanofiltration; Thin-film composite membranes; Aminated lignin; Interfacial polymerization; Thermodynamic Modeling and Molecular Dynamics

Journal Pre-proof

1. Introduction

The transition toward low-carbon energy systems has intensified global attention on the secure supply and recovery of critical minerals [1,2]. Lithium demand has risen rapidly because of its widespread use in batteries for electric vehicles and large-scale energy storage systems [3,4], and is projected to increase substantially to meet future climate targets [5]. Salt-lake brines represent an important alternative lithium resource because of their relatively simple processing routes and lower operational costs compared with ore-based extraction [6,7]. However, conventional evaporation-based recovery raises concerns regarding water consumption and ecosystem disruption, while the low Li^+ concentration and high Mg^{2+}/Li^+ ratio of many brines make selective separation difficult because of the similar physicochemical characteristics and hydrated dimensions of Li^+ and Mg^{2+} [8,9].

Direct lithium extraction technologies (DLE), including adsorption, ion exchange, membrane separation, and electrochemical processes, have therefore received increasing attention [1,10]. Among these approaches, nanofiltration (NF) is attractive because of its operational simplicity and scalability [11,12]. Commercial NF membranes are commonly based on polyamide thin-film composite structures fabricated through interfacial polymerization between PIP and TMC [13–15], but their Li^+/Mg^{2+} selectivity remains limited because they were primarily designed for water softening [16–18]. Li^+/Mg^{2+} separation can be improved by regulating the charge and effective pore structure of the PA layer [12,19,20]. Accordingly, many recent studies have introduced amine-rich components to increase the positive charge density of the selective layer and strengthen electrostatic exclusion of Mg^{2+}. However, excessive incorporation of highly reactive amines can accelerate interfacial polymerization and produce an overly dense PA

network. In systems based on strongly amine-rich polymers such as PEI, this densification may restrict the transport of both Li^+ and Mg^{2+} and reduce water permeability [21,22]. These limitations have motivated recent studies to explore more controlled amine-containing additives, introduced either during selective-layer formation or through post-modification, to regulate interfacial polymerization while avoiding excessive PA-network densification.

These additives are typically incorporated into the aqueous phase during interfacial polymerization to regulate monomer diffusion, tailor PA morphology, and introduce additional cationic functionalities [23,24]. For instance, amine-functionalized covalent organic frameworks (COFs) used as additives during interfacial polymerization have enabled the fabrication of lithium-selective PA membranes with a high water permeance of 19.6 L m^{-2} h^{-1} bar^{-1} and a Li^+/Mg^{2+} separation factor of up to 21.3 [25]. Similarly, amine-functionalized inorganic nanoparticles, such as TiO_2, have been shown to participate in PA formation by restricting amine monomer diffusion, reducing excessive crosslinking, and increasing membrane positive charge, resulting in a water permeance of 9.65 L m^{-2} h^{-1} bar^{-1} and a Li^+/Mg^{2+} selectivity of 16.3 [26]. Carbon-based amine-functionalized additives, including aminated graphene quantum dots (GQDs-NH_2), have also been shown to integrate into the PA network, enhancing cationic charge density and modifying the selective-layer morphology, thereby simultaneously improving water permeability and Li^+/Mg^{2+} separation performance [27]. Similar improvements have been reported using dopamine-modified graphitic carbon nitride incorporated during interfacial polymerization [28]. Beyond carbon-based systems, amine–functionalized metal–organic frameworks (MOFs) [29,30], *star*-shaped block copolymers (SPs) [31], and polypeptide dendrimers [32] have also been incorporated into the PA layer, where their porous structures and

amine functionalities enhance Li^+/Mg^{2+} selectivity, in some cases approaching complete Mg^{2+} rejection.

Despite these advances, most reported additives are synthetic nanomaterials that require energy-intensive synthesis and incur high material and processing costs, raising concerns about scalability and long-term sustainability [33,34]. Lignin offers a promising bio-based alternative as a charge-regulating modifier. It is an abundant aromatic biopolymer produced in large quantities as a by-product of the pulp, paper, and bioethanol industries, and contains a high density of reactive functional groups that enable straightforward chemical functionalization to introduce cationic sites [35]. Its renewable origin, wide availability, and low cost make lignin an attractive precursor for the development of sustainable membrane additives [36]. However, native lignin exhibits significant structural heterogeneity and broad molecular-weight distributions, which can lead to inconsistent performance when used directly. Fractionation addresses this limitation by isolating lignin fractions with narrower molecular-weight distributions and more uniform functional-group content. In particular, low-molecular-weight fractions enriched in phenolic groups provide enhanced accessibility for subsequent amination [37,38]. In our previous work, lowering the fractionation pH was shown to reduce lignin molecular weight while increasing phenolic hydroxyl content [39], making the low-pH fraction particularly suitable for further functionalization. This insight guided the selection of the lignin fraction used in the present study.

In this study, aminated lignin (AL) was introduced into the piperazine-containing aqueous phase during interfacial polymerization to fabricate lithium-selective thin film composite (TFC) NF membranes. As a renewable and scalable source of amine functionalities, AL enables regulation of membrane charge while remaining compatible with PA formation, avoiding the high cost,

energy intensity, and potential leaching associated with inorganic nanofillers. AL incorporation simultaneously influences membrane charge, hydrophilicity, and PA layer formation, providing a sustainable strategy for improving Li^+/Mg^{2+} selectivity.

Although lignin derivatives have been explored in desalination and water purification membranes [35,40–42], their use in lithium separation remains very limited, and the application of aminated lignin for selective Li^+/Mg^{2+} separation has not been systematically investigated.

Here, we present a simple molecular engineering strategy in which AL is introduced as a bio-based reactive additive into the PIP-containing aqueous phase to regulate PIP transport and its interfacial polymerization with TMC, thereby tailoring the structure and separation properties of the resulting PA selective layer for enhanced Li^+/Mg^{2+} separation. Membrane physicochemical properties were systematically characterized, and separation performance and stability were evaluated under simulated brine conditions. Furthermore, conductor-like screening model for real solvents (COSMO-RS) calculations and molecular dynamics (MD) simulations were performed to elucidate the role of AL in modulating PIP transport and interfacial polymerization behavior. The results show that AL alters the thermodynamic and interfacial environment of PIP and suppresses its interfacial diffusion, leading to a heterogeneous distribution of monomers. The membranes exhibited significantly enhanced lithium selectivity, demonstrating the potential of this approach for lithium recovery from salt-lake brines.

2. Experimental methods

2.1. Materials

TFC membranes were fabricated on a polyethersulfone (PES) support membrane (0.03 μm pore size, Sterlitech Corporation). For the fabrication of TFC membranes, piperazine (PIP, ≥99%),

trimesoyl chloride (TMC, 98%), and n-hexane (≥99%) were obtained from Sigma-Aldrich. To determine the membrane molecular weight cut-off (MWCO), polyethylene glycol (PEG) with molecular weights of 200, 400, 600, and 1000 g/mol (Sigma-Aldrich) was used. Softwood kraft lignin (SKL) was obtained from West Fraser Timber Co. (Hinton, AB, Canada). 2-Chloroethylamine hydrochloride, obtained from Sigma Aldrich, was used for the amination of lignin. To evaluate membrane performance, various salts were used, including lithium chloride (LiCl, ≥99%), sodium chloride (NaCl, ≥99%), potassium chloride (KCl, ≥99%), magnesium chloride hexahydrate ($MgCl_2 \cdot 6H_2O$, ≥99%), calcium chloride ($CaCl_2$, ≥99%), sodium sulfate (Na_2SO_4, ≥99%), and magnesium sulfate ($MgSO_4$, ≥99%) (Fisher Scientific).

2.2. Amination of lignin

Softwood kraft lignin was fractionated following our previously reported procedure. Among the resulting fractions, the B4 fraction, precipitated at pH 3.1 and previously characterized with a viscosity-average molecular weight of approximately 500 g mol^{-1}, was selected for subsequent amination with 2-chloroethylamine under alkaline conditions [39] (see **Figure 1**). Briefly, the fractionated lignin was dissolved in an aqueous sodium hydroxide solution under stirring until a homogeneous solution was obtained. 2-chloroethylamine was then added, and the mixture was heated to 80 °C under reflux with continuous stirring for 24 h to promote nucleophilic substitution. After completion, the reaction mixture was acidified to approximately pH 3 to precipitate the AL. The solids were recovered by centrifugation, washed repeatedly with deionized water to remove residual salts and unreacted species, and dried under vacuum at 40 °C overnight [43].

2.3. Membrane fabrication

An ultrathin PA layer was fabricated on a PES substrate via interfacial polymerization using PIP and AL in the aqueous phase and TMC in the organic phase. The aqueous phase contained 0.5 wt% PIP. For the pristine membrane, the aqueous solution contained only PIP, whereas for the modified membranes, AL was added at concentrations of 0.15, 0.25, and 0.35 wt%. The aqueous solution was poured onto the PES substrate and allowed to remain for 2 min to ensure complete saturation, after which the excess solution was removed using a polymethacrylic roller. Subsequently, 0.15 wt% TMC dissolved in n-hexane was introduced to initiate interfacial polymerization, and the reaction was allowed to proceed for 1 min. The resulting membranes were then heated at 80 °C for 5 min to complete the polymerization. The PIP and TMC concentrations were selected based on fabrication conditions previously optimized by our research group [44], which provided a continuous PA-selective layer and a suitable balance between water permeability and Li^{+}/Mg^{2+} separation performance. The membranes containing 0.00, 0.15, 0.25, and 0.35 wt% AL were designated Pristine, M-0.15, M-0.25, and M-0.35, respectively. **Figure 1** presents a schematic of the membrane fabrication process.

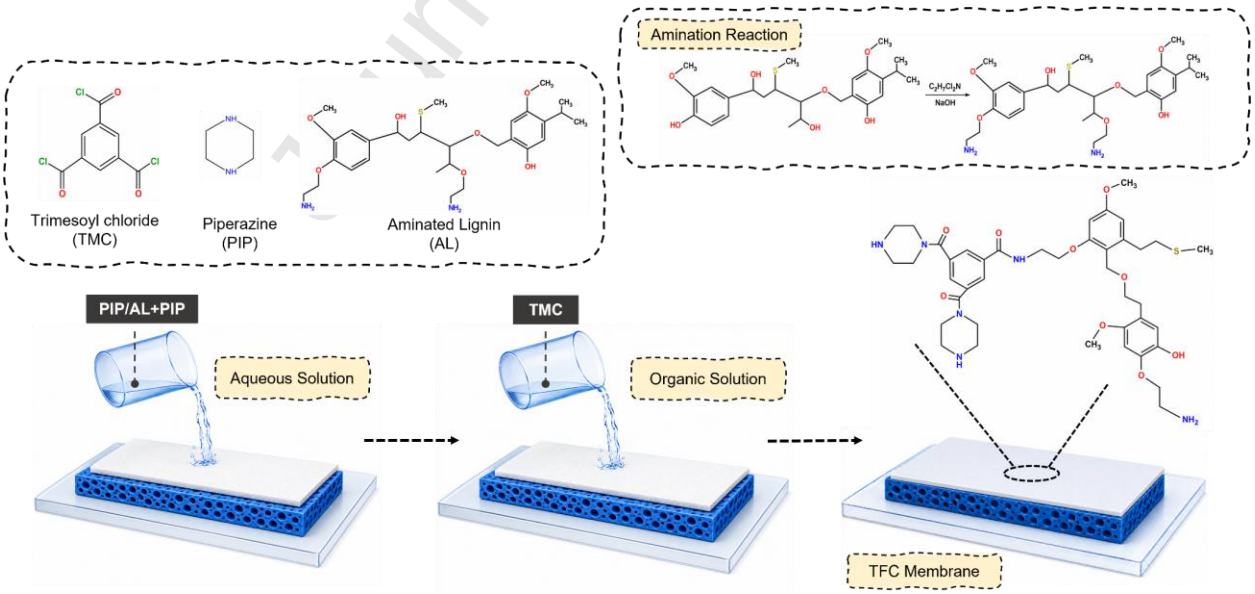


Figure 1. Schematic illustration of the amination reaction and the fabrication procedure for the TFC membranes.

2.4. Computational details

2.4.1. COSMO-RS calculations

The computational procedure followed a methodology previously reported in the literature [45]. Molecular structures were obtained either from the COSMObase database (lowest-energy conformers) or constructed using TmoleX within TURBOMOLE for AL, PIP, and TMC. Geometry optimizations were carried out using TURBOMOLE (v4.5.2) at the BP86/TZVP level in the gas phase and under the COSMO solvation model. Frequency analyses were performed to confirm that all optimized structures correspond to true minima. The resulting .energy and .cosmo files were used as inputs for COSMO-RS calculations, performed with COSMOtherm (v25, COSMOthermX interface) using the BP_TZVP_25 parameterization. σ-profiles were generated to analyze surface charge distributions, while the activity coefficient (γ) of PIP was calculated for aqueous mixtures containing the corresponding experimental AL concentrations (0, 0.15, 0.25, and 0.35 wt%). Partition coefficients (log P) between the aqueous and organic phases were also calculated to assess changes in the thermodynamic behavior and phase preference of PIP [46].

2.4.2. MD Simulations

MD simulations were carried out in GROMACS version 2026.1 [46] using the CHARMM36 force field. Small-molecule topologies were generated using CHARMM-GUI [47]. A biphasic simulation box ($6 \times 6 \times 12$ nm^3) was constructed using Packmol [48], consisting of an aqueous phase (4800 water molecules, TIP3P model) and an organic phase (750 hexane molecules). One PIP molecule and one AL molecule were initially placed in the aqueous phase, establishing a highly dilute solute concentration of approximately 7.7 mM within this phase. Energy

minimization was first conducted using the steepest-descent method, after which the system was equilibrated for 200 ps under the canonical (NVT) ensemble and for 2 ns in the isothermal-isobaric (NPT) ensemble. During equilibration, the PIP molecule was restrained in the bulk aqueous phase using harmonic position restraints.

For all dynamic simulations, an integration time step of 2 fs was used with hydrogen bonds constrained using the LINCS algorithm [49]. Electrostatic interactions were computed using the Particle Mesh Ewald (PME) method with a real-space cutoff of 1.2 nm. Van der Waals interactions were smoothly switched off between 1.0 and 1.2 nm using a force-switch modifier. The temperature was maintained at 298.15 K using the velocity-rescaling (V-rescale) thermostat [50]with a coupling constant of 1.0 ps. For NPT equilibration, the pressure was regulated at 1.0 bar using the C-rescale barostat with an isotropic coupling constant of 5.0 ps and a compressibility of 4.5×10^{-5} bar^{-1}.

To generate initial configurations for umbrella sampling, steered molecular dynamics (SMD) was performed by pulling the PIP molecule along the z-axis from the center of the bulk water region (z = 0 nm) toward the center of the bulk hexane phase (z = 5.4 nm) at a constant velocity of 1 nm ns^{-1} using a harmonic spring constant of 1000 kJ mol^{-1} nm^{-2}. Umbrella sampling simulations were then conducted using 54 windows uniformly spaced along the reaction coordinate. Each window was equilibrated for 100 ps and subsequently simulated for 5 ns in the NVT ensemble using a harmonic force constant of 1000 kJ mol^{-1} nm^{-2}. The potential of mean force (PMF) profile was calculated from the umbrella sampling data using the Weighted Histogram Analysis Method (WHAM) [51]. To quantify the hindering effect of aminated lignin on solute transport, position-dependent diffusion coefficients D(z) were estimated within each

umbrella window using the autocorrelation function method. Based on the formalism outlined by Hummer [52], the local diffusion coefficient is calculated from the coordinate's variance and its integrated autocorrelation time τ_z under the harmonic bias:

$$D(z) = \frac{var(z)}{\tau_z} \quad (1)$$

2.5. AL and membrane characterization

The fractionated lignin precursor and the resulting AL were characterized by ATR-FTIR over 500-4000 cm^{-1} and by quantitative ^{31}P NMR spectroscopy using a 500 MHz Varian instrument. Prior to ^{31}P NMR analysis, the hydroxyl groups were phosphitylated according to an established method [53]. Hydroxyl groups were quantified from their corresponding chemical-shift regions relative to an internal standard, and hydroxyl conversion was determined from the relative decrease in total hydroxyl content after amination. The PA selective layer was characterized by XPS using a Kratos AXIS ULTRA system (0-1100 eV), and the spectra were analyzed with CasaXPS software. The TFC membrane surface and internal structures were examined via field-emission scanning electron microscopy (FESEM, Hitachi S-4800) and transmission electron microscopy (TEM, Philips/FEI Morgagni 268). Surface roughness was determined over a 10 μm^2 scan area using a Veeco Dimension 3100 AFM in tapping mode, with an amplitude setpoint under 0.6 V and a scan rate of 0.4 Hz. The AFM measurements were conducted using probes with an estimated tip radius of 8 nm and a cantilever spring constant of 5 N/m. AFM data were processed using Nanoscope Analysis. Zeta potential measurements were performed using a SurPASS 3 electrokinetic analyzer (Anton Paar) to evaluate the membrane surface charge. The zeta potential was measured three times per sample, and the average was reported. Contact angle measurements were performed using the sessile drop method (Kruss DSA 100, GmbH,

Germany) to assess membrane surface wettability. A 2 μL drop of deionized water was placed on the membrane surface. For each membrane, at least 10 droplets were analyzed, and the mean value was recorded.

A 200 ppm PEG solution was used to assess the MWCO of the TFC membranes. The MWCO was defined as the PEG molecular weight corresponding to approximately 90% rejection. PEG solutions were filtered for 1 h at 70 psi, and the permeate concentrations were determined by total organic carbon (TOC) analysis using a Shimadzu TOC-L analyzer. To evaluate potential AL leaching during long-term operation, permeate collected from the 168 h stability test was also analyzed by TOC.

2.6. Membrane performance tests

Membrane flux and rejection were evaluated in a cross-flow filtration system operated at 25 °C and 70 psi. The effective separation area of the NF membranes was 20.6 cm^2. The feed solution had an initial pH of 6.5. Feed solution compositions for NF performance testing are reported in the captions of the respective figures. All membrane-performance measurements were performed in triplicate (n=3). Water flux (J) was calculated as follows:

$$J = \frac{V}{A\Delta t} \quad (2)$$

where V corresponds to the permeate volume (L), A to the effective membrane area (m^2), and Δt to the operation time (h). The rejection of solutes was determined according to the following expression:

$$R(\%) = \left(1 - \left(\frac{C_p}{C_f}\right)\right) \times 100 \quad (3)$$

C_p and C_f represent the solute concentrations in the permeate and feed, respectively. The selectivity (S) for Li^+/Mg^{2+} was calculated using the following equation:

$$S_{Li^+/Mg^{2+}} = \left(\frac{C_{Li,p}/C_{Mg,p}}{C_{Li,f}/C_{Mg,f}}\right) \quad (4)$$

Single-salt rejection was evaluated by measuring solution conductivity with an electrical conductivity meter (AR50, Fisher Scientific). Mixed salt concentrations were measured using a Thermo iCAP6300 Duo ICP-OES (Thermo Fisher Scientific).

3. Results and discussion

3.1. Characterization of the AL

ATR-FTIR was used to characterize the AL and confirm successful amination (**Figure 2a**). A broad band between 3200 and 3500 cm^{-1} corresponds to N-H stretching vibrations of amine groups, while the band at 1250 cm^{-1} is attributed to C-N stretching. N-H bending vibrations of amine groups are observed at 1600-1650 cm^{-1}. A significant reduction in the phenolic C-O stretching band at 1106-1134 cm^{-1} in the AL spectrum suggests substitution of phenolic hydroxyl groups by amine functionalities, thereby confirming successful amination [43,54].

To further confirm the structural modification induced by amination, quantitative ^{31}P NMR analysis was conducted on lignin and AL. The unmodified lignin exhibited a total hydroxyl content of 1.9 mmol g^{-1} (**Figure 2b** and **Table 1**). After amination, 86.4% of the hydroxyl groups were converted, confirming the effectiveness of the functionalization process. The remaining unreacted hydroxyl groups were predominantly located in the aliphatic region and are attributed to impurities present in the original lignin sample, likely originating from co-extracted fatty acids or resinous components introduced during the supplier's extraction and recovery processes. The

residual aliphatic hydroxyl content was 0.12 mmol g^{-1}, while terminal carboxylic acid moieties and guaiacyl units together accounted for approximately 0.14 mmol g^{-1} (each ≈ 0.07 mmol g^{-1}) [55].

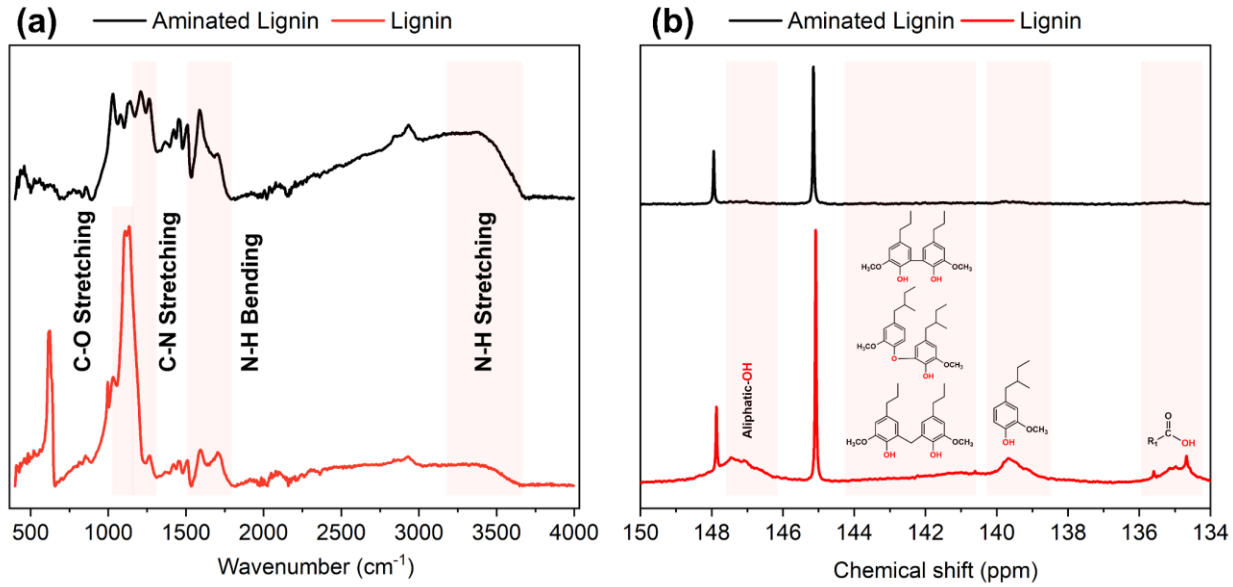


Figure 2. (a) FTIR and (b) quantitative ^{31}P NMR spectra of lignin and AL, illustrating chemical changes associated with amination.

Table 1. Hydroxyl contents of lignin and AL.

Hydroxyl groups	**Lignin (mmol g^{-1})**	**%**	**AL (mmol g^{-1})**	**%**
Carboxylic Acids	0.17	8.7	0.07	27.2
Non-Condensed	0.64	33.3	0.07	27.0
Condensed	0.37	19.6	0.00	0.00
Aliphatic	0.73	38.4	0.12	45.8
Total	1.91	100.0	0.26	100.0

3.2. Membrane Characterization

XPS analysis with high-resolution C 1s and N 1s spectra was employed to investigate the surface chemical structure and bonding environments of the pristine and M-0.25 membranes. The quantitative fitting results are provided in **Table 2**, and the corresponding spectra are shown in **Figure 3**. The C 1s spectra were primarily composed of C-C/C-H (285 eV), C-N (286.2 eV), and N-C=O (288.0 eV) components in both samples. A distinct O-C=O (288.8 eV) contribution associated with free carboxyl groups was observed for the pristine membrane, whereas this component decreased markedly to 0.30% in M-0.25 and was only detected through curve fitting. This reduction suggests that acyl chloride groups from TMC participated in amide bond formation with AL amine groups during interfacial polymerization. To further examine this effect, the ratio of O-C=O to N-C=O species in the C 1s spectrum was calculated. A lower O-C=O/N-C=O ratio reflects a higher degree of reaction between acyl chlorides and amines since residual carboxyl species are mainly formed through hydrolysis of unreacted acyl chlorides. The M-0.25 membrane displayed a distinctly smaller ratio than the pristine sample, indicating more extensive formation of amide linkages and fewer residual carboxylic species. The N 1s spectra of the pristine and M-0.25 were deconvoluted into three components corresponding to N-C=O (400.5 eV), C-N (399.6 eV), and R-NH_3^+/R_2-NH_2^+(402 eV). After incorporation of AL, the relative fraction of protonated amine species increased from 2.83% in the pristine membrane to 7.47% in the M-0.25 membrane, likely due to the introduction of additional amine functionalities by AL and their protonation under the fabrication conditions [56–58].

Table 2. Deconvoluted peak area percentages of functional groups obtained from high-resolution XPS C 1s and N 1s spectra for pristine and M-0.25 membranes.

	C 1s species (%)	N 1s species (%)

Sample	C-C/ C-H	C-COOH/C-CON	C-N	N-C=O	O-C=O	O-C=O / N-C=O	C–N	N-C=O	$R\text{-}NH_3^+$/ $R_2\text{-}NH_2^+$
Pristine	47.47	4.91	28.84	16.20	2.57	0.158	87.41	9.77	2.83
M-0.25	52.76	6.06	26.8	14.08	0.30	0.021	78.93	13.60	7.47

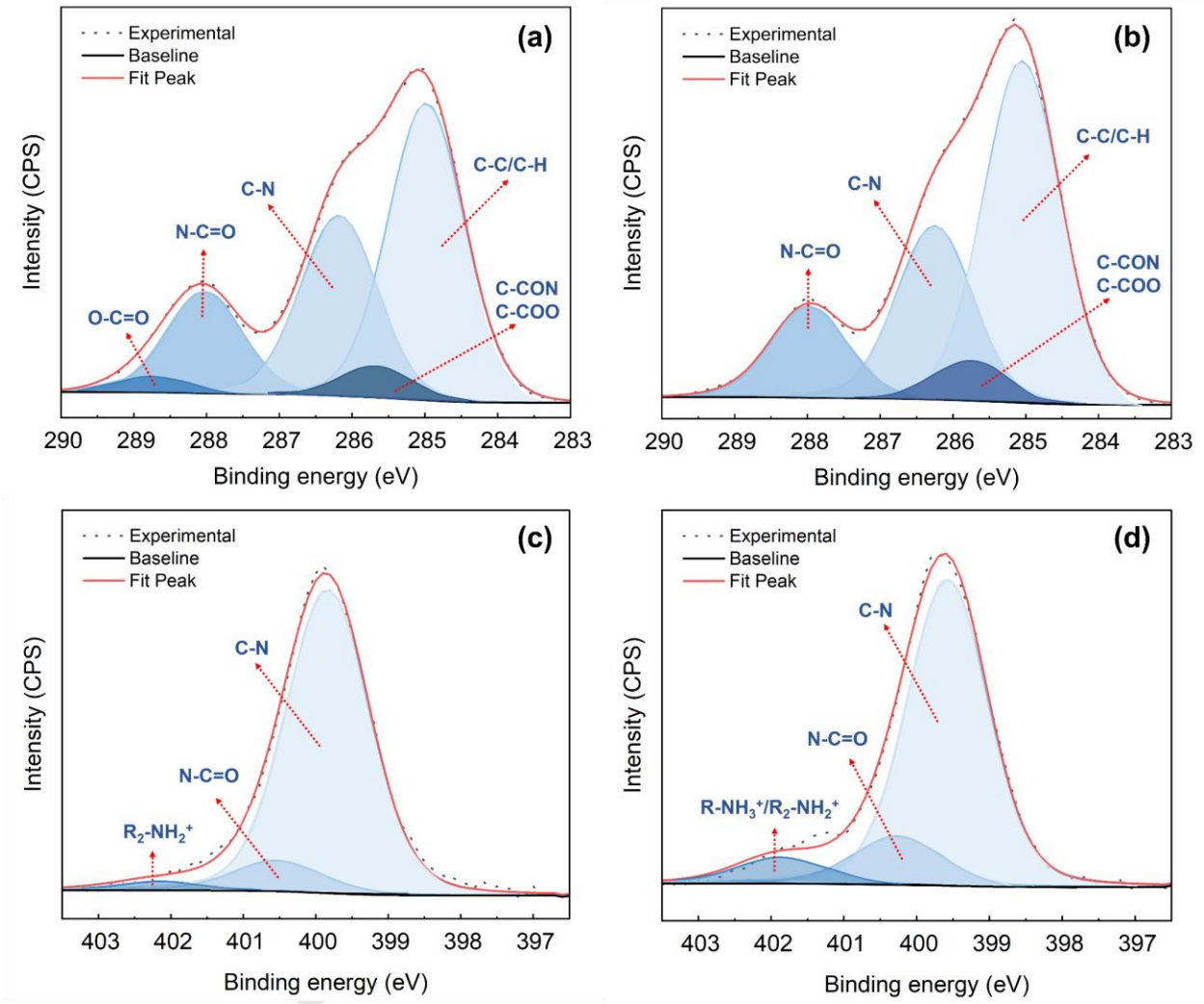


Figure 3. High-resolution XPS spectra of C 1s for (a) pristine and (b) M-0.25, and N 1s for (c) pristine and (d) M-0.25 membranes.

Figure 4a presents top-view SEM images of the pristine and M-0.25 membranes, revealing a clear contrast in surface morphology. The pristine membrane shows a relatively smooth top layer, whereas M-0.25 shows a rougher architecture with more pronounced nodular features, consistent with AL incorporation in the PA layer. During interfacial polymerization, amine

groups on the AL react with acyl chloride groups of TMC to form amide linkages, anchoring the AL within the PA network.

Cross-sectional SEM and TEM images (**Figures 4b,c**) show an ultrathin PA selective layer formed atop a sponge-like porous support. The modified membrane exhibits a reduced PA thickness, decreasing from approximately 58.3 ± 1.55 nm for the pristine membrane to about 30.2 ± 1.33 nm for M-0.25.

AFM analysis (**Figure 4d**) further quantified surface topography. The pristine membrane showed an average roughness (R_a) of 10.7 ± 2.1 nm and a root-mean-square roughness (R_q) of 14.2 ± 1.8 nm. Following AL incorporation, roughness increased, with M-0.25 exhibiting R_a and R_q values of 15.7 ± 1.9 nm and 19.6 ± 2.2 nm, respectively. These results align with SEM observations, confirming increased surface roughness in the modified membrane.

The observed morphological changes indicate that AL substantially influences interfacial polymerization at the aqueous-organic interface. The experimentally observed concentration-dependent increase in aqueous-phase viscosity following AL addition (Section S2, Supporting Information), together with the MD results showing reduced PIP mobility near the aqueous-organic interface, indicates that AL modifies the monomer-transport environment during interfacial polymerization. These changes in monomer transport and interfacial distribution may alter local polymerization kinetics, thereby contributing to enhanced lateral nodular development while limiting vertical PA growth. Consequently, these transport-regulation effects are consistent with the formation of a thinner and rougher selective layer [40,41].

Journal Pre-proof

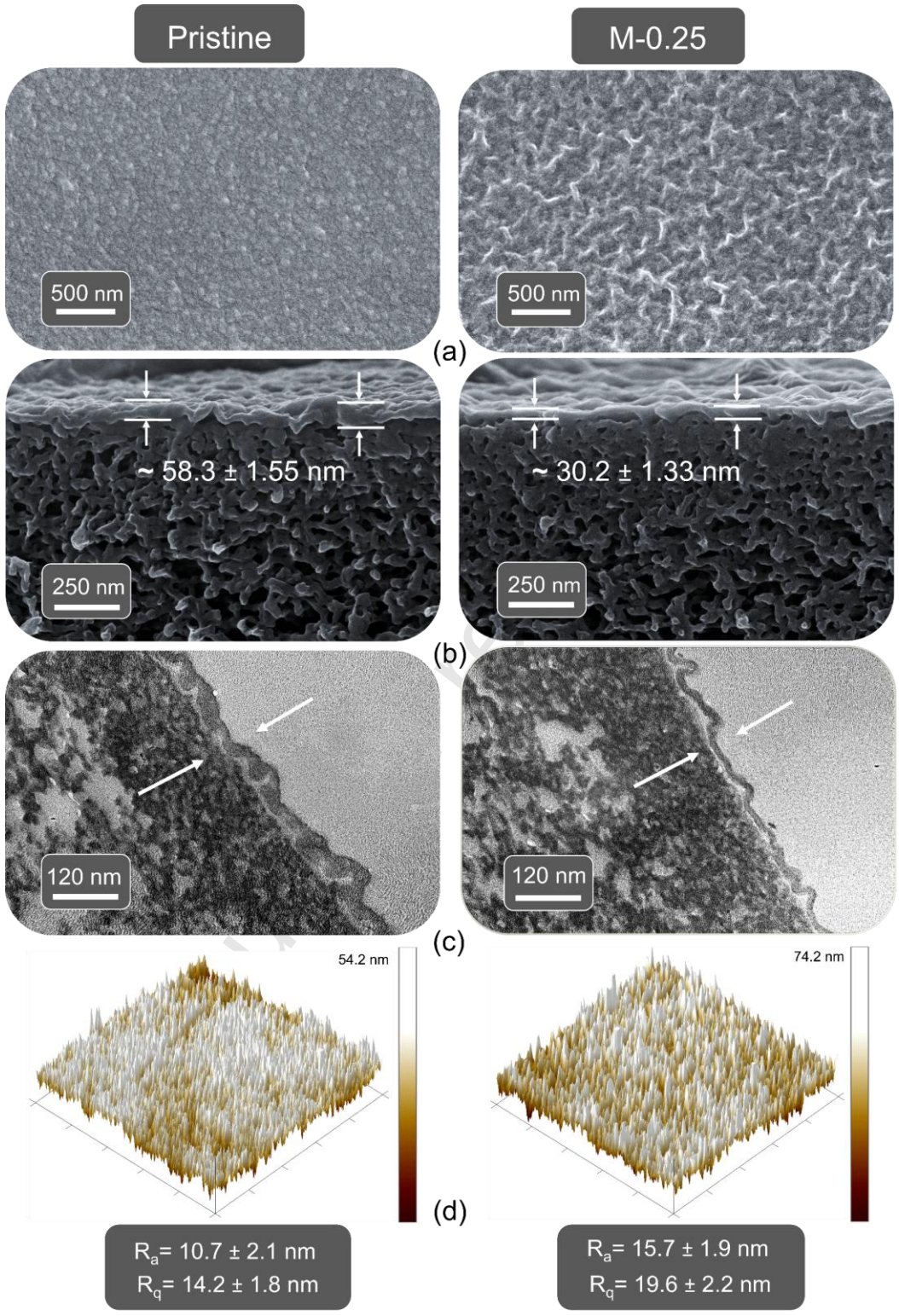


Figure 4. Morphological characterization of pristine and AL-modified (M-0.25) membranes. (a) Top-view SEM images. (b) Cross-sectional SEM images. (c) TEM images of the selective layer. (d) AFM surface topography images showing roughness changes after modification.

To investigate the proposed mechanism at the molecular level, COSMO-RS calculations and MD simulations were employed. The COSMO-RS results (**Figure 5a**) reveal a small but systematic concentration-dependent trend in the thermodynamic behavior of PIP in the aqueous phase upon increasing AL concentration. Specifically, ln(γ) decreases from -0.420 to -0.432, while log P decreases from -1.010 to -1.025 as the AL concentration increases from 0 to 0.35 wt%. Although these variations are small and may approach the numerical sensitivity of the method, their monotonic evolution indicates a consistent trend toward slightly more favorable stabilization of PIP in the AL-containing aqueous environment. Here, γ represents the activity coefficient, which quantifies deviations from ideal-solution behavior; values of $\gamma < 1$ indicate favorable interactions and solute stabilization in the given phase. In this case, $\gamma_{PIP} \sim 0.65$ confirms that PIP is thermodynamically stabilized in the aqueous phase. The parameter P denotes the partition coefficient between the organic and aqueous phases ($P = C_{organic}/C_{aqueous}$), where log P < 0 indicates a preference for the aqueous phase. The observed decrease in log P therefore suggests that PIP becomes slightly more hydrophilic and less likely to partition into the organic phase in the presence of AL.

The calculated thermodynamic descriptors (**Table 3**) further support this behavior. The chemical potential of PIP decreases slightly ($\Delta\mu \approx -0.0065$ kcal mol^{-1}) with increasing AL concentration, indicating a gradual stabilization of PIP in the aqueous phase. This trend is accompanied by a small but systematic decrease in the van der Waals contribution ($\Delta H_{vdW} \approx -0.0036$ kcal mol^{-1}), while the hydrogen-bonding term remains consistently negative (≈ -6.67 kcal mol^{-1}) with only marginal variation. The misfit contribution remains essentially unchanged. These results suggest that both hydrogen-bonding and van der Waals interactions govern PIP-AL association, albeit with complementary roles. Hydrogen bonding provides a consistently strong stabilizing

framework, whereas the incremental changes induced by AL addition primarily manifest as subtle variations in van der Waals interactions. Thus, while hydrogen bonding dominates the overall interaction strength, dispersion-type interactions appear to play a key role in modulating the thermodynamic response to AL incorporation.

This interpretation is consistent with the σ-profiles (**Figure 5b**), where AL exhibits a broad amphiphilic distribution spanning both hydrogen-bond donor and acceptor regions, whereas PIP displays a narrower profile centered near neutral σ values. Partial overlap in the hydrogen-bonding regions suggests specific interactions, while substantial overlap in the near-neutral region confirms the dominant role of van der Waals interactions. Collectively, these interactions likely promote transient associations between PIP and AL, thereby reducing PIP's effective tendency to partition into the organic phase. In the context of interfacial polymerization with TMC, such associations may influence the transport of PIP toward the reaction interface, thereby influencing polymerization kinetics and selective layer formation.

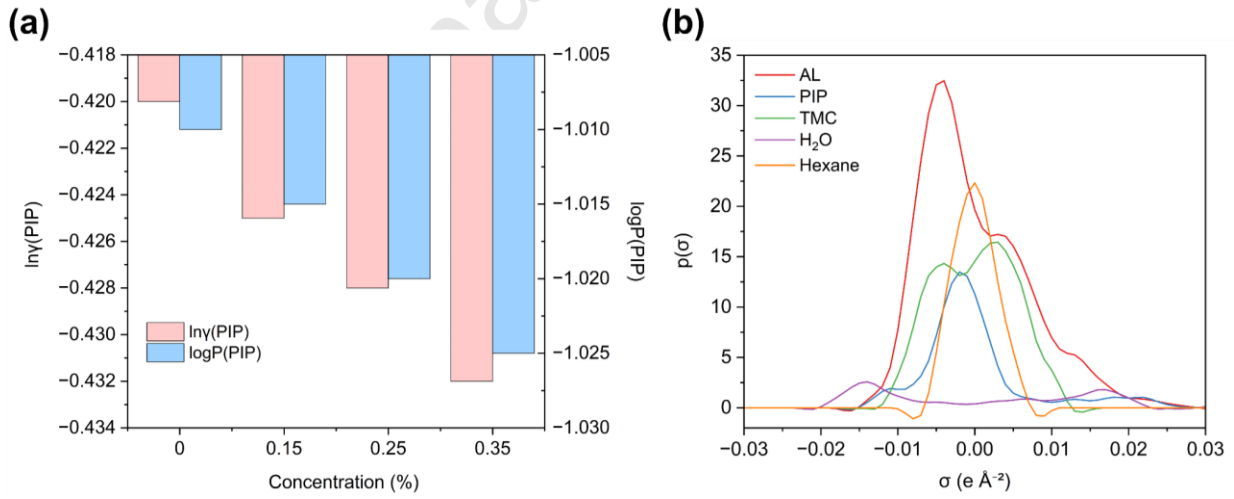


Figure 5. COSMO-RS analysis of the effect of AL on the thermodynamic behavior of PIP in the aqueous phase. (a) Variation of lnγ and log P with AL concentration (0 to 0.35 wt%). (b) σ-profiles of AL, PIP, TMC, H_2O, and hexane, showing their polarity distributions and intermolecular interaction regions.

Table 3. COSMO-RS-derived thermodynamic descriptors of PIP in the aqueous phase at different AL concentrations (0.00–0.35 wt%). The chemical potential (μ) and the contributions to the excess enthalpy from misfit interactions (H_{MF}), hydrogen bonding (H_{HB}), and van der Waals interactions (H_{vdW}) are reported.

AL Concentration	μ (kcal/mol)	H_{MF} (kcal/mol)	H_{HB} (kcal mol^{-1})	H_{vdW} (kcal mol^{-1})
0.00%	2.8813	2.2344	-6.6769	-5.5709
0.15%	2.8785	2.2336	-6.6763	-5.5725
0.25%	2.8766	2.2331	-6.6760	-5.5735
0.35%	2.8747	2.2326	-6.6756	-5.5745

Building on thermodynamic insights from COSMO-RS, MD simulations were performed to investigate interfacial transport behavior. The potential of mean force (PMF) profile (**Figure 6a**), derived from steered MD simulations, exhibits an energy minimum at the aqueous-organic interface, indicating that PIP preferentially accumulates at the phase boundary regardless of the presence of AL. The depth of this minimum is comparable under both conditions, suggesting the absence of strong long-lived PIP-AL complexation under the simulated highly dilute conditions. Despite the absence of stable complexation, diffusion analysis (**Figure 6b**) shows that while PIP mobility in the bulk aqueous phase remains largely unchanged, its diffusion coefficient at the interface decreases in the presence of AL. Although these localized calculations exhibit inherent statistical noise, a clear spatial trend is visible: a more pronounced drop in diffusion occurs both just before ($z \approx 1.7$-1.9 nm) and just after ($z \approx 3.2$ nm) the interface when AL is present. In these boundary regions, the diffusion coefficient drops to a minimum of approximately 0.2 nm^2 ns^{-1} compared to roughly 0.6 nm^2 ns^{-1} for the pristine baseline. These values are of the same order of magnitude as PIP diffusion coefficients reported for related lignin-regulated systems [41]. This reduction indicates that AL creates a high-friction interfacial environment that hinders PIP mobility near the phase boundary. The AL mass density profile along the z-axis (**Figure S1** in the ESI) shows that this species also concentrates at the aqueous-organic boundary, competing

with PIP by occupying part of the interface volume otherwise available for diffusion and reaction. Thus, the slower PIP diffusion in the AL-containing system is attributed to interfacial crowding from AL accumulation near the aqueous-organic interface, together with the experimentally observed increase in aqueous-phase viscosity, rather than to strong, long-lived AL-PIP complexation. Differences between the COSMO-RS and MD analyses may partly arise from the highly dilute conditions used in the MD simulations and limitations of the classical non-polarizable CHARMM36 force field, which does not explicitly account for electronic polarization. Nevertheless, these findings indicate that AL acts as a transport modulator rather than a complete inhibitor. During TMC-based interfacial polymerization, this regulation likely limits PIP transport toward the reaction interface, enabling more controlled PA film development.

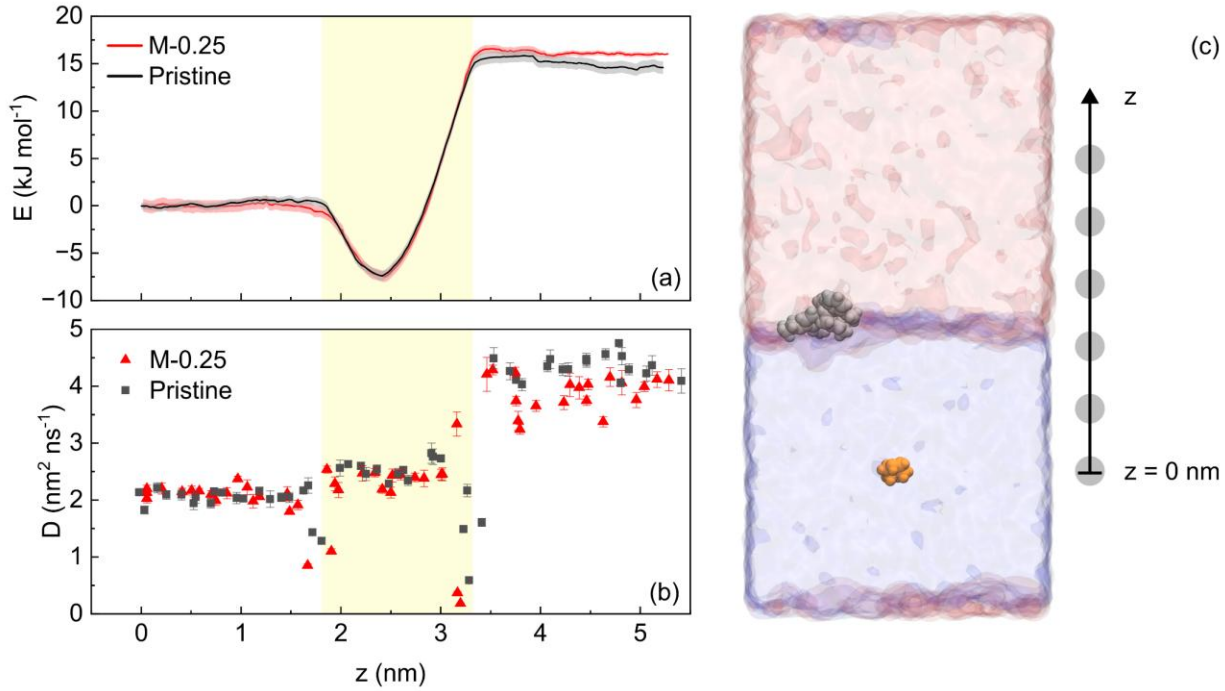


Figure 6. Molecular dynamics results for PIP transport across the aqueous–organic interface for pristine and M-0.25 systems: (a) PMF profiles and (b) position-dependent diffusion coefficients (*D*) as a function of the reaction

coordinate *z*. The yellow shaded region indicates the approximate water-hexane interface. Panel (c) shows a schematic of the MD simulation configuration: the organic phase (red), aqueous phase (blue), AL near the interface (grey), and PIP in the aqueous phase (orange). The shaded interfacial region represents the proposed high-friction environment associated with the presence of AL near the aqueous–organic boundary. The vertical arrangement illustrates the umbrella-sampling windows along the *z* reaction coordinate, starting from $z = 0$ nm.

The surface wettability of the pristine and M-0.25 membranes was assessed by water contact angle measurements (**Figure 7a**). Wettability plays a critical role in NF performance, as stronger membrane-water interactions generally promote higher water permeability. The pristine membrane exhibited a hydrophilic surface with a contact angle of 61.2° ± 1.8°, attributed to carboxyl groups formed by hydrolysis of unreacted acyl chlorides from TMC. After AL incorporation, the contact angle decreased significantly to 32.5° ± 1.3° in M-0.25, indicating enhanced hydrophilicity. This improvement arises from the hydrophilic functional groups in AL, which promote hydrogen bonding with water molecules [59].

The surface charge characteristics of the membranes were evaluated by zeta potential measurements (**Figure 7b**). The M-0.25 membrane exhibited a higher zeta potential than the pristine membrane, indicating reduced surface negativity. This shift can be attributed to the primary amine functional groups in AL, which influence the membrane charge through two mechanisms. First, some amine groups react with acyl chlorides during interfacial polymerization, thereby limiting the formation of negatively charged carboxyl groups upon hydrolysis. Second, protonation of residual amine groups in aqueous media generates positively charged ammonium species. Together, these effects account for the observed shift toward a less negative surface potential.

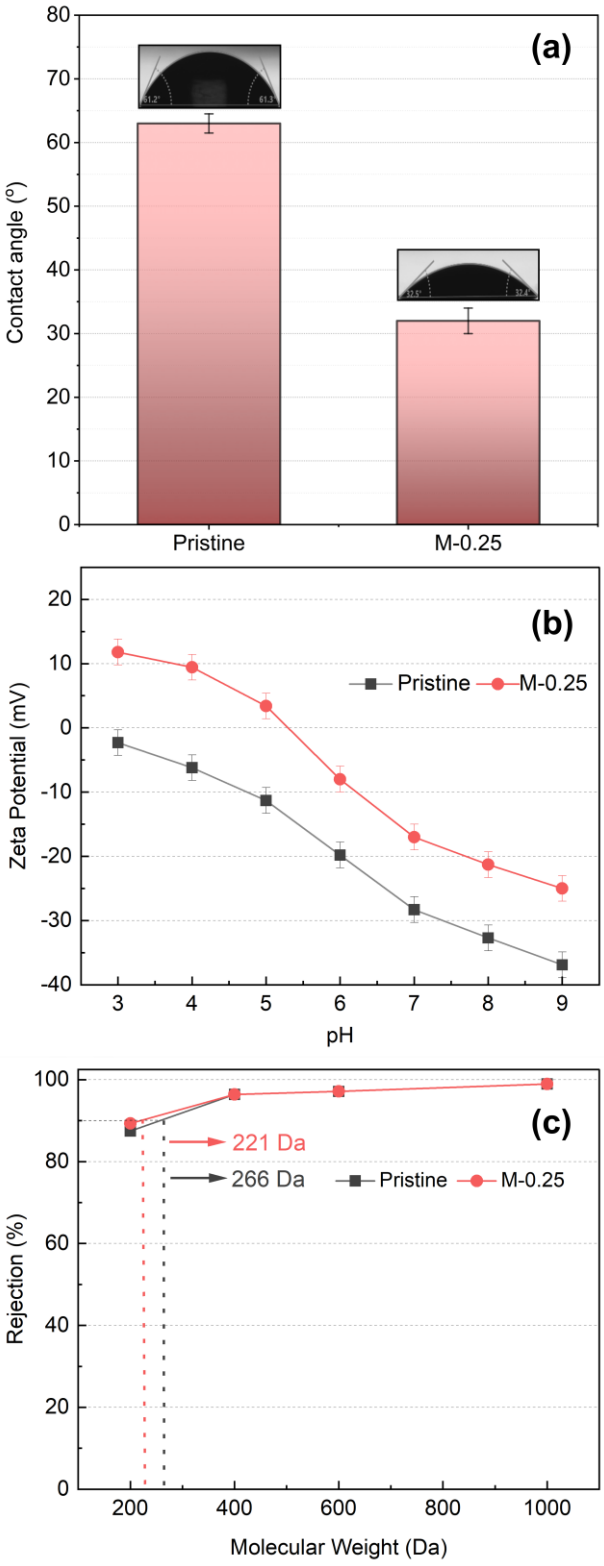


Figure 7. (a) Water contact angle measurements, (b) zeta-potential profiles, and (c) molecular weight cut-off (MWCO) of the pristine and M-0.25 membranes.

Figure 7c shows that AL modification decreases the MWCO from 266 Da for the pristine membrane to 221 Da for M-0.25, indicating enhanced molecular-sieving behavior following AL incorporation. To further assess structural changes, we performed water-uptake and gravimetric porosity measurements. Water uptake decreased slightly from 53.64% for the pristine membrane to 51.50% for M-0.25, while the corresponding gravimetric porosity decreased from approximately 31% to 27%. Notably, despite the enhanced hydrophilicity of M-0.25, no increase in water uptake was observed. Together with the reduction in water-accessible porosity, these results are consistent with reduced accessible void volume and a more restrictive transport structure after AL incorporation. Detailed experimental procedures and calculations are provided in the Supporting Information.

3.3. Membrane performance

The effect of AL incorporation on membrane performance was evaluated relative to the pristine membrane. As shown in **Figure 8a**, all AL-containing membranes exhibited more negative Li^+ rejection values in a mixed feed solution (Li^+/Mg^{2+} mass ratio 1:20, total concentration 2000 ppm), indicating enhanced Li^+ transport through the selective layer. Among them, the membrane containing 0.25 wt% AL (M-0.25) demonstrated the most favorable separation performance. It achieved a Mg^{2+} rejection of 96.7%, significantly higher than the 78% rejection of the pristine membrane, while simultaneously improving Li^+ permeability (Li^+ rejection of -69% compared to -51.7%). Consequently, the Li^+/Mg^{2+} selectivity increased to 51.2, corresponding to a 7.4-fold improvement over the unmodified membrane ($S_{Li^+/Mg^{2+}}$ = 6.89). These results confirm that AL integration effectively enhances monovalent-divalent ion separation, with M-0.25 identified as the optimal formulation.

To clarify whether the performance enhancement originated from lignin amination rather than from the lignin backbone alone, a concentration-matched control membrane was prepared using 0.25 wt% unmodified lignin under otherwise identical fabrication conditions. The unmodified-lignin membrane exhibited a modest improvement over the pristine membrane but remained markedly inferior to M-0.25, with a water flux of 38.7 L m^{-2} h^{-1}, Li^+ rejection of -56.7 %, Mg^{2+} rejection of 85%, and Li^+/Mg^{2+} selectivity of 10.45. These results suggest that the lignin backbone may exert a limited influence on membrane formation, whereas the introduced amine functionalities provide the dominant additional contribution to the enhanced separation performance of M-0.25.

The enhanced Li^+/Mg^{2+} selectivity of M-0.25 can be understood through the coupled effects of ion size, hydration energetics, steric confinement, and ion partitioning within the selective layer. Ion transport through a sub-nanometer PA matrix is highly sensitive to both the effective pore structure and the hydration characteristics of the permeating ions. Mg^{2+} has a larger hydrated diameter than Li^+, approximately 0.86 and 0.76 nm, respectively, and a substantially more negative hydration free energy, approximately -1828 and -515 kJ mol^{-1}, respectively [60]. Consequently, the more restrictive transport structure of M-0.25, together with the larger hydrated size and higher dehydration penalty of Mg^{2+}, imposes a greater barrier to Mg^{2+} transport through the selective layer.

Surface-charge effects also influence ion partitioning within the PA matrix. AL incorporation introduces protonatable amine functionalities and reduces the abundance of residual carboxylic species, as supported by the XPS results and the less-negative zeta potential of M-0.25. The more negatively charged pristine membrane may therefore favor greater electrostatic partitioning of

Mg^{2+} into the selective layer, whereas this interaction is weakened in M-0.25. The markedly higher Mg^{2+} rejection thus arises from the combined effects of the more restrictive transport structure of M-0.25, the higher dehydration penalty of Mg^{2+}, and less favorable Mg^{2+} partitioning within the AL-containing PA matrix.

The AL-modified membranes achieved enhanced selectivity while maintaining favorable water permeability. The pristine and M-0.25 membranes exhibited comparable water fluxes of 41 and 40.2 L m^{-2} h^{-1}, respectively. Despite its reduced PA-layer thickness and enhanced hydrophilicity, M-0.25 did not exhibit a corresponding increase in water flux. The hydrophilic functionalities of AL enhance water affinity [61], while AL-mediated regulation of monomer diffusion produces a thinner selective layer, both of which favor water permeation. However, AL incorporation during interfacial polymerization modifies the composition and organization of the resulting PA network, which may introduce additional resistance to water transport. The reduction in gravimetric porosity from approximately 31% to 27%, together with the slight decrease in water uptake despite the enhanced hydrophilicity of M-0.25, provides supporting evidence of a more restrictive transport structure. Therefore, the comparable water flux likely results from a balance between the favorable effects of enhanced water affinity and reduced transport distance and the more restrictive transport characteristics of the AL-containing PA matrix.

The separation trend in mixed-ion experiments was consistent with that observed in single-salt tests conducted at 1000 ppm (**Figure 8b**). Mg^{2+} rejection increased from 68.6% for the pristine membrane to 93% for M-0.25, confirming that AL incorporation strengthens divalent ion exclusion.

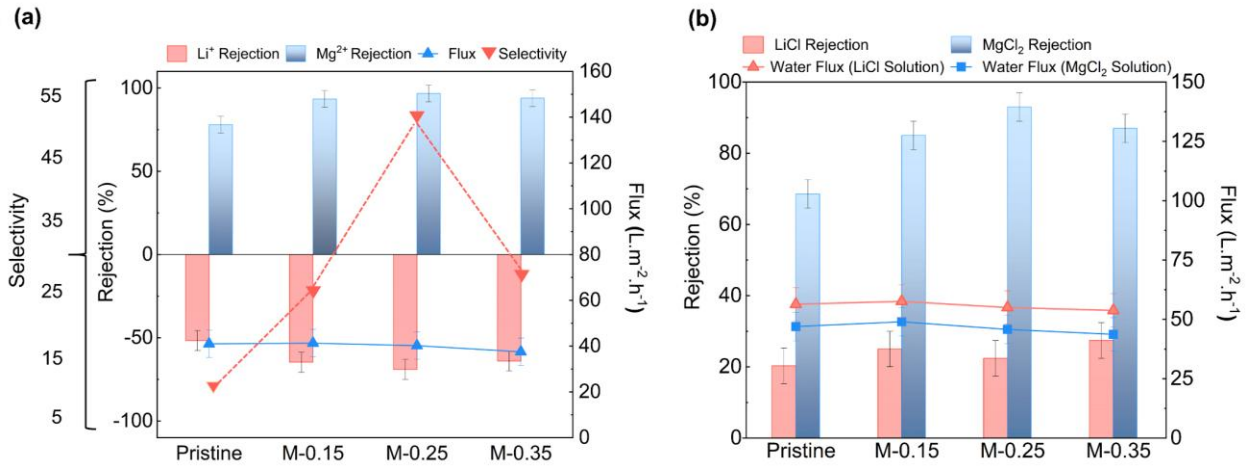


Figure 8. Separation performance of the membranes evaluated in (a) mixed salt solutions with a total concentration of 2000 ppm and a Li^+/Mg^{2+} ratio of 1:20, and (b) single salt solutions composed of 1000 ppm LiCl or $MgCl_2$.

The negative Li^+ rejection corresponds to a permeate-to-feed Li^+ concentration ratio of 1.69, indicating approximately 69% Li^+ enrichment in the permeate relative to the feed. This result demonstrates the preferential transport of Li^+ over Mg^{2+} through the M-0.25 membrane. The use of a lignin-derived additive may also offer material and sustainability advantages for membrane fabrication, while further process-scale studies are needed to evaluate lithium recovery and economic performance under practical operating conditions.

Figure 9a shows the effect of feed concentration on the separation behavior of the M-0.25 membrane. Increasing the salt concentration from 1000 to 5000 ppm resulted in a gradual decrease in water flux for both LiCl and $MgCl_2$ solutions, consistent with the increase in feed osmotic pressure at higher salt concentrations ($J = A\ (\Delta P - \Delta\pi)$), where A is the hydraulic permeability of the membrane. The different flux trends observed for LiCl and $MgCl_2$ likely reflect the combined effects of their different molar concentrations at a given mass concentration, ionic strength, membrane-ion interactions, salt rejection, and concentration polarization. In

addition, increasing the concentration of each salt increases ionic strength, which can enhance charge screening and concentration polarization near the membrane surface. These concentration- and salt-specific effects can alter the local salt concentration and osmotic pressure at the membrane interface, thereby reducing the effective driving force for water permeation and influencing the observed water flux.

A slight reduction in the rejection of both Li^+ and Mg^{2+} was observed with increasing feed concentration. This behavior is attributed to enhanced charge screening and intensified concentration polarization at higher ionic strength. Charge screening alters ion partitioning within the selective layer, while increased ion accumulation near the membrane surface strengthens concentration polarization and facilitates ion transport across the membrane. Consequently, Mg^{2+} rejection decreases more noticeably, whereas Li^+, as a monovalent ion, is less sensitive to these effects [62].

Figure 9b shows the influence of the Mg^{2+}/Li^+ mass ratio on the separation performance of the M-0.25 membrane at a fixed total concentration of 2000 ppm. Mg^{2+} rejection remained consistently high (above 96%) across all ratios, whereas Li^+ rejection varied substantially. This behavior can be attributed to changes in ionic strength and coupled ion transport within the mixed-salt system. Increasing the Mg^{2+}/Li^+ mass ratio raises the ionic strength, which enhances charge screening and alters ion partitioning within the selective layer. Mg^{2+} rejection remains relatively stable because its transport is strongly restricted by steric confinement and its high dehydration penalty, even at higher ionic strength. In contrast, Li^+ transport is more strongly influenced by electroneutrality constraints. To maintain charge balance, Li^+ permeation may be promoted alongside Cl^- transport through the membrane, and this effect becomes more

pronounced as the Mg^{2+} fraction increases. Consequently, Li^{+} rejection decreases, while Mg^{2+} rejection remains high, resulting in an increase in Li^{+}/Mg^{2+} selectivity from 29.6 at a mass ratio of 1:1 to 58.8 at 100:1.

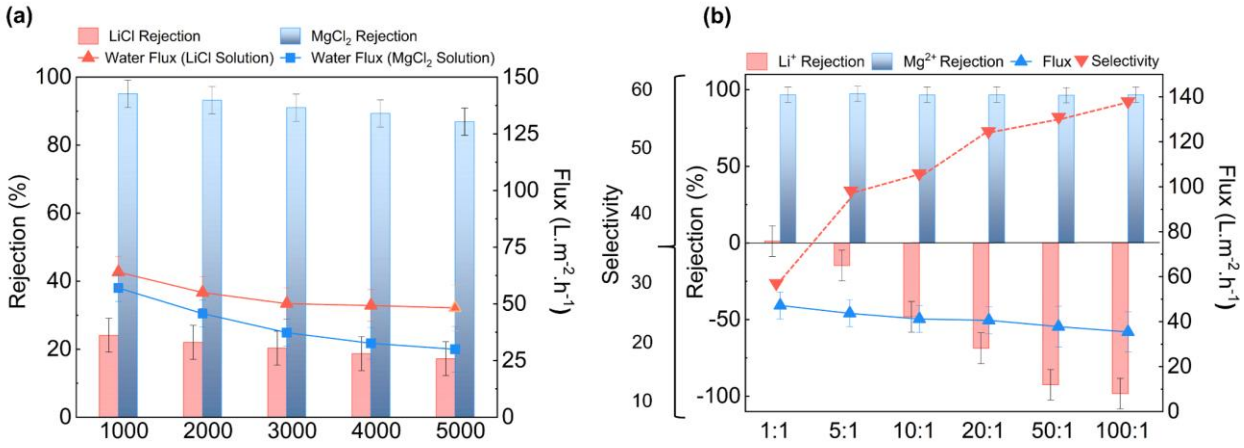


Figure 9. Effect of (a) salt concentration utilizing separate LiCl and $MgCl_2$ feed solutions and (b) Mg^{2+}/Li^{+} ratio at constant total salt concentration of 2000 ppm on the performance of optimized M-0.25 membrane.

Figure 10a presents the separation behavior of M-0.25 in single-salt solutions (1000 ppm) containing LiCl, NaCl, KCl, $MgCl_2$, $CaCl_2$, Na_2SO_4, and $MgSO_4$. The membrane exhibited low rejection toward monovalent salts (LiCl: 22%, NaCl: 21.2%, KCl: 19.3%), whereas substantially higher rejection was recorded for divalent cation salts ($MgCl_2$: 93.3%, $CaCl_2$: 82%). The relatively low rejection of Li^{+}, Na^{+}, and K^{+} is further attributed to their physicochemical properties that favor transport through nanopores. First, their smaller hydrated diameters (Li^{+}: 0.764 nm, Na^{+}: 0.716 nm, K^{+}: 0.662 nm) reduce steric resistance compared to Mg^{2+} (0.856 nm) and Ca^{2+} (0.824 nm). Second, monovalent cations possess substantially less negative hydration free energies (Li^{+}: -515, Na^{+}: -364, K^{+}: -295 kJ mol^{-1}) compared with Mg^{2+} (-1828 kJ mol^{-1}) and Ca^{2+} (-1504 kJ mol^{-1}), enabling easier dehydration and faster transport across the selective layer.

The higher rejection of Mg^{2+} relative to Ca^{2+} is consistent with its larger hydration radius and more negative hydration free energy.

Anion identity also significantly influenced separation performance. The rejection of chloride salts (NaCl: 21.2% and $MgCl_2$: 93.3%) was lower than that of sulfate salts (Na_2SO_4: 98.1% and $MgSO_4$: 97.5%). Because M-0.25 is negatively charged under the tested conditions, SO_4^{2-} experiences stronger electrostatic exclusion and less favorable partitioning into the PA selective layer than Cl^-. This electrostatic effect is considered the primary factor responsible for the higher sulfate rejection. In addition, SO_4^{2-} has a larger hydrated diameter and a substantially more negative hydration free energy than Cl^-, with values of 0.758 nm and -1145 kJ mol^{-1} for SO_4^{2-} compared with 0.648 nm and -363 kJ mol^{-1} for Cl^-. These differences further increase the steric and dehydration barriers to SO_4^{2-} transport. In contrast, the smaller hydrated size and weaker hydration of Cl^- facilitate its permeation and the coupled transport of counter-cations required to maintain electroneutrality. Therefore, the sulfate/chloride rejection difference is governed primarily by electrostatic exclusion, while hydrated size and dehydration energetics provide additional contributions. These rejection trends are consistent with the measured flux behavior [60,63].

Monovalent salts, which permeate more readily, yielded higher water fluxes (55.3, 56.7, and 57.2 L m^{-2} h^{-1} for LiCl, NaCl, and KCl, respectively), whereas salts containing divalent ions produced lower fluxes (46.1, 48.2, 42.8, and 44.1 L m^{-2} h^{-1} for $MgCl_2$, $CaCl_2$, Na_2SO_4, and $MgSO_4$, respectively). These differences in water flux likely reflect the combined effects of salt-specific osmotic pressure, ion rejection, and membrane-ion interactions.

Journal Pre-proof

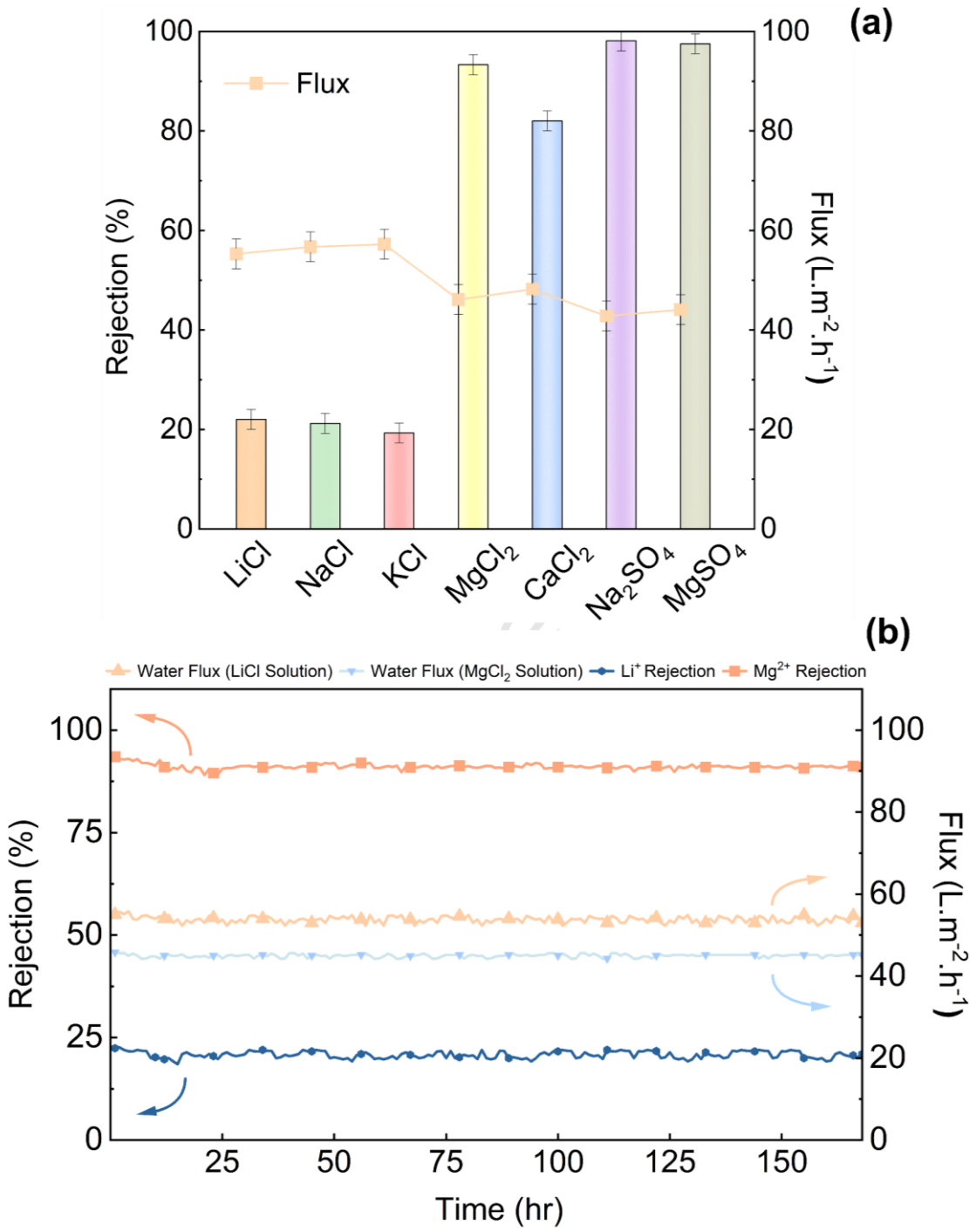


Figure 10. Filtration performance of the M-0.25 membrane: (a) ion separation behavior in single-salt solutions (1000 ppm), including LiCl, NaCl, KCl, $MgCl_2$, $CaCl_2$, Na_2SO_4, and $MgSO_4$; (b) long-term stability during operation in LiCl and $MgCl_2$ solutions (1000 ppm each).

Figure 10b shows that M-0.25 maintained stable permeate flux and ion-rejection performance over 168 hours of continuous operation in 1000 ppm LiCl and $MgCl_2$ solutions, indicating good operational stability. To further assess the stability of AL incorporation, permeate collected at the end of the long-term filtration test was analyzed by TOC. The TOC concentration remained below the detection limit, indicating that no detectable organic carbon attributable to AL leaching was observed under the tested conditions.

Table 4 compares the performance of M-0.25 with representative Li^+/Mg^{2+}-selective NF membranes evaluated under comparable binary-feed conditions, using a total salt concentration of 2000 ppm and an Mg^{2+}/Li^+ mass ratio of 20:1. As summarized in Table 4 and illustrated in Figure 11, M-0.25 exhibits the highest Li^+/Mg^{2+} selectivity among the compared membranes, reaching 51.2. The literature membranes show selectivities ranging from 8.0 to 41.6, with water permeance values between 8.0 and 24.5 L m^{-2} h^{-1} bar^{-1}. Although several reported membranes provide higher water permeance than M-0.25, their Li^+/Mg^{2+} selectivity remains lower. M-0.25 therefore occupies a favorable region of the permeance-selectivity landscape, combining competitive water permeance of 8.4 L m^{-2} h^{-1} bar^{-1} with markedly enhanced ion discrimination. This comparison demonstrates that the improved selectivity of M-0.25 is achieved without a severe loss of water transport performance.

Beyond the permeance-selectivity comparison, most previously reported Li^+/Mg^{2+}-selective NF membranes employ post-modification, interlayers, or specialized functional components, including crown ethers, Cyclen, graphene oxide, carbon nitride, quaternary ammonium compounds, covalent organic framework interlayers, and charged nanoparticles. These strategies can improve ion selectivity through coordination, size-sieving, or electrostatic interactions, but

they may also require multistep fabrication, specialized reagents, or careful control of additive dispersion and interfacial compatibility. In comparison, AL is a bio-based modifier derived from renewable lignin resources that is introduced directly into the aqueous phase during interfacial polymerization. The M-0.25 membrane therefore combines high Li^+/Mg^{2+} selectivity with a comparatively simple modification route and avoids the need for post-treatment or additional interlayer fabrication, offering potential advantages for cost-effective and scalable membrane preparation.

Table 4. Comparison of the water permeance and Li^+/Mg^{2+} selectivity of M-0.25 with previously reported NF membranes evaluated using binary LiCl/$MgCl_2$ feeds with a total salt concentration of 2000 ppm and an Mg^{2+}/Li^+ mass ratio of 20:1.

NF membrane	Water Permeance(L $m^{-2}h^{-1}bar^{-1}$)	$S_{Li^+/Mg^{2+}}$	Reference
M-0.25	8.4	51.2	This study
PES/PIP-TMC/F-SiO_2NPs	11.6	37.9	[21]
PES/PIP/TMC-ARG/GLA	9.8	17.1	[44]
PSF/PEI-15C5/TMC	8.0	11.9	[64]
PES-GO/PEI/TMC	11.1	16.1	[65]
PSF/PEI-Cyclen/TMC	14.0	8.0	[66]
PES/PEI-g-C_3N_5/TMC	9.8	18.2	[67]
PSF/PEI-GRT/TMC	16.8	22.7	[68]
PES/TAEA-BPTAB/TMC	23.5	24.8	[69]
PEI/TMC-BAPE	24.5	41.6	[70]
PES/TpPa-SO_3H/PEI-TMC	10.7	21.5	[71]
PEI-EC/SG	13.0	27.7	[72]

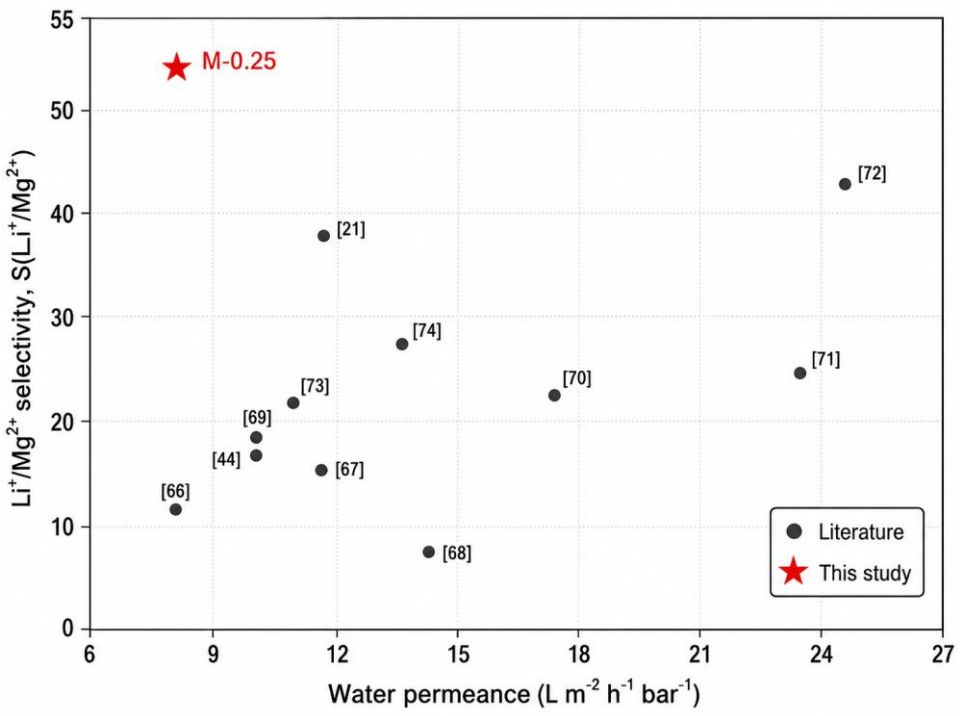


Figure 11. Benchmark comparison of the water permeance and Li^+/Mg^{2+} selectivity of the M-0.25 membrane with previously reported nanofiltration membranes. The comparison is based on binary LiCl/$MgCl_2$ feeds with a total salt concentration of 2000 ppm and an Mg^{2+}/Li^+ mass ratio of 20:1. Literature data and corresponding references are summarized in Table 4.

4. Conclusion

This study demonstrates that incorporating AL during PA formation is an effective strategy for fabricating NF membranes with high Li^+/Mg^{2+} selectivity, making them promising candidates for lithium recovery from magnesium-rich brines. AL was synthesized via alkaline SN2 nucleophilic substitution of fractionated lignin using 2-chloroethylamine as the functionalizing agent. The structural and chemical characteristics of the modified membranes were verified through comprehensive analyses, including XPS, SEM, TEM, AFM, zeta potential, and water contact angle measurements. COSMO-RS calculations and MD simulations demonstrate that AL

simultaneously alters the thermodynamic state of PIP in the aqueous phase and reduces its interfacial mobility, revealing coupled thermodynamic and kinetic control over monomer transport. This regulation slows monomer delivery to the reaction zone, enabling a more controlled interfacial polymerization process. Consequently, excessive vertical growth of the PA layer is mitigated, while lateral network development is favored, resulting in a thinner selective layer with higher surface roughness. AL incorporation increased membrane hydrophilicity and altered the chemical and charge environment of the PA layer. The enhanced Mg^{2+} rejection was attributed to the combined effects of a more restrictive selective-layer transport structure, the higher dehydration penalty of Mg^{2+}, and altered Mg^{2+} partitioning within the PA matrix. Among the fabricated samples, M-0.25 exhibited the optimal performance, combining high Mg^{2+} rejection with enhanced Li^{+} permeation. In a 2000 ppm mixed-salt solution (Li^{+}/Mg^{2+} mass ratio = 1:20), M-0.25 achieved 96.7% Mg^{2+} rejection and -69% Li^{+} rejection, delivering a water flux of 40.2 L $m^{-2}h^{-1}$ and a Li^{+}/Mg^{2+} selectivity of 51.2. In contrast, the pristine membrane showed a selectivity of only 6.89 at a comparable water flux. Overall, these findings demonstrate that incorporating AL into PA formation provides a bio-based materials-design strategy for producing NF membranes with high Li^{+}/Mg^{2+} selectivity and supports further investigation of this approach for lithium recovery from brine resources.

Journal Pre-proof

Acknowledgments

The financial support for this work by the Natural Sciences and Engineering Research Council of Canada (NSERC), Canada's Oil Sands Innovation Alliance (COSIA), and Alberta Innovates is gratefully acknowledged.

This work was developed within the scope of the project CICECO Aveiro Institute of Materials, UIDB/50011/2020 (DOI: 10.54499/UIDB/50011/2020), UIDP/50011/2020 (DOI:

10.54499/UIDP/50011/2020), UID/50011/2025 (DOI: 10.54499/UID/50011/2025), and LA/P/0006/2020 (DOI: 10.54499/LA/P/0006/2020), financed by national funds through FCT/MCTES (PIDDAC). Filipe H. B. Sosa acknowledges FCT, Fundação para a Ciência e a Tecnologia, I.P., for the researcher contract CEECIND/07209/2022 (DOI: 10.54499/2022.07209.CEECIND/CP1720/CT0019) under the Scientific Employment Stimulus Individual Call 2022. André Nogueira acknowledges FCT, Fundação para a Ciência e a Tecnologia, I.P., for project/grant 2023.01418.BD (DOI: 10.54499/2023.01418.BD).

Declaration of Competing Interest

The authors declare no competing interests.

Data Availability

Data will be made available on request.

References

[1] Y. Feng, Y. Zhu, W. Chen, X. Huang, X. Weng, M.D. Meyer, T.H. Chen, Y. Liu, Z. He, C.H. Hou, K. Zuo, N.Y. Yip, K. Gong, J. Lou, Q. Li, A rationally designed scalable thin film nanocomposite cation exchange membrane for precise lithium extraction, Nature Communications 16 (2025). https://doi.org/10.1038/s41467-025-63660-3.

[2] X. Yao, Q. Zheng, V.T. Tjambiru, P. Wu, Z. Li, A. Miyamoto, M. Watanabe, High-Selectivity Separation of Lithium from Spent Lithium-Ion Battery Leachates Using Surface-Modified Commercial Nanofiltration Membranes, Environ. Sci. Technol. 59 (2025). https://doi.org/10.1021/acs.est.5c05864.

[3] D. Yang, Y. Yang, T. Wong, S. Iguodala, A. Wang, L. Lovell, F. Foglia, P. Fouquet, C. Breakwell, Z. Fan, Y. Wang, M.M. Britton, D.R. Williams, N. Shah, T. Xu, N.B. McKeown, M.M. Titirici, K.E. Jelfs, Q. Song, Solution-processable polymer membranes with hydrophilic subnanometre pores for sustainable lithium extraction, Nature Water 3 (2025). https://doi.org/10.1038/s44221-025-00398-8.

[4] Y. Shi, Z. Mai, K. Guan, B. Li, Q. Shen, Q. Song, W. Fu, S. Xiang, R. Takagi, H. Matsuyama, Nanomorphogenesis of interlayered polyamide membranes for precise ion sieving in lithium extraction, Water Res. 274 (2025). https://doi.org/10.1016/j.watres.2024.123063.

[5] L. Kong, G. Yan, K. Hu, Y. Yu, N. Conte, K.R. Mckenzie, M.J. Wagner, S.G. Boyes, H. Chen, C. Liu, X. Liu, Electro-driven direct lithium extraction from geothermal brines to generate battery-grade lithium hydroxide, Nature Communications 16 (2025). https://doi.org/10.1038/s41467-025-56071-x.

[6] H. Kim, J. Choi, H. Kim, S. Jeon, J.H. Lee, Structural tailoring of poly(quaternary ammonium) thin-film composite membranes for efficient lithium recovery from concentrated salt-lake brine, J. Memb. Sci. 733 (2025). https://doi.org/10.1016/j.memsci.2025.124333.

[7] Q. Fan, J. Lin, Y. Sun, X. Hu, H. Yu, Z. Lu, In situ polyamide nanofiltration coatings for enhanced lithium extraction from high Mg/Li brines, Chemical Engineering Journal 523 (2025). https://doi.org/10.1016/j.cej.2025.168375.

[8] L. Gui, S. Wang, L. Chen, Y. Dou, Y. Fan, S. Huang, T. Wu, X. Tian, Crumpled polyethyleneimine nanofiltration membranes regulated by thermocapillary effect for efficient magnesium-lithium separation, Water Res. 287 (2025). https://doi.org/10.1016/j.watres.2025.124352.

[9] M.L. Vera, W.R. Torres, C.I. Galli, A. Chagnes, V. Flexer, Environmental impact of direct lithium extraction from brines, Nat. Rev. Earth Environ. 4 (2023). https://doi.org/10.1038/s43017-022-00387-5.

[10] J. Farahbakhsh, F. Arshadi, Z. Mofidi, M. Mohseni-Dargah, C. Kök, M. Assefi, A. Soozanipour, M. Zargar, M. Asadnia, Y. Boroumand, V. Presser, A. Razmjou, Direct lithium extraction: A new paradigm for lithium production and resource utilization, Desalination 575 (2024). https://doi.org/10.1016/j.desal.2023.117249.

[11] W. Ji, Y. Li, F. Duan, L. Liu, R. Cao, J. Yin, H. Sun, J. Luo, H. Cao, Maintaining high magnesium/lithium selectivity in nanofiltration at high salinity: optimizing membrane charge distribution for synergistic Donnan and ion adhesion effects, J. Memb. Sci. 729 (2025). https://doi.org/10.1016/j.memsci.2025.124160.

[12] J. Zhai, A. Balogun, S. Bhattacharjee, R.J. Vogler, R. Khare, M. Malmali, A. Deonarine, Y. xiao Shen, Nanofiltration as pretreatment for lithium recovery from salt lake brine, J. Memb. Sci. 710 (2024) 123150. https://doi.org/10.1016/J.MEMSCI.2024.123150.

[13] Y. Liang, Y. Zhu, C. Liu, K.R. Lee, W.S. Hung, Z. Wang, Y. Li, M. Elimelech, J. Jin, S. Lin, Polyamide nanofiltration membrane with highly uniform sub-nanometre pores for sub-1 Å precision separation, Nat. Commun. 11 (2020). https://doi.org/10.1038/s41467-020-15771-2.

[14] L. Wang, Y. Lin, Y. Tang, D. Ren, X. Wang, Fabrication of oppositely charged thin-film composite polyamide membranes with tunable nanofiltration performance by using a piperazine derivative, J. Memb. Sci. 634 (2021). https://doi.org/10.1016/j.memsci.2021.119405.

[15] Y. Li, S. Wang, H. Li, G. Kang, Y. Sun, H. Yu, Y. Jin, Y. Cao, Preparation of highly selective nanofiltration membranes by moderately increasing pore size and optimizing microstructure of polyamide layer, J. Memb. Sci. 643 (2022). https://doi.org/10.1016/j.memsci.2021.120056.

[16] Y. Zhang, Y. Fan, G. Zhou, Y. Cao, J. Wang, X. Jiang, N. Zhang, S. Yin, Based on high cross-linked structure design to fabricate PEI-based nanofiltration membranes for Mg2+/Li+ separation, J. Memb. Sci. 693 (2024). https://doi.org/10.1016/j.memsci.2023.122351.

[17] S. Duan, S. Jiang, Z. Li, P. Zhang, K. Guan, P. Xu, H. Matsuyama, Low-temperature regulated interfacial polymerization of nanofiltration membrane for efficient Li+/Mg2+ separation, Desalination 597 (2025) 118393. https://doi.org/10.1016/J.DESAL.2024.118393.

[18] S. Fang, K. Guan, S. Zhou, Q. Song, Y. Shi, W. Fu, Z. Li, P. Xu, M. Hu, Z. Mai, P. Zhang, H. Matsuyama, Ternary-coordination-regulated polyamide nanofiltration membranes for Li+/Mg2+ separation, Desalination 581 (2024) 117577. https://doi.org/10.1016/J.DESAL.2024.117577.

[19] P. Xu, K. Guan, Y.H. Chiao, Z. Mai, Z. Li, M. Hu, P. Zhang, R.R. Gonzales, H. Matsuyama, Fine-tuning polyamide nanofiltration membrane for ultrahigh separation selectivity of Mg2+ and Li+, J. Memb. Sci. 688 (2023). https://doi.org/10.1016/j.memsci.2023.122133.

[20] D.P.A. Sudarmaja, C.E. Suryanaga, V.S.H. Sujoto, S.N.A. Jenie, W. Astuti, F. Anggara, A. Prasetya, Sutijan, H.T.B.M. Petrus, Enhancing lithium concentration performance from synthetic geothermal brine through electro-nanofiltration method, Chemical Engineering Journal 516 (2025). https://doi.org/10.1016/j.cej.2025.164134.

[21] A. Aghaei, M.A. Islam, E. Jashni, A. Khalili, J.-Y. Cho, M. Sadrzadeh, Efficient Lithium Recovery from Water Using Polyamide Thin-Film Nanocomposite (TFN) Membrane Modified with Positively Charged Silica Nanoparticles, ACS Appl. Mater. Interfaces 16 (2024) 66514–66531. https://doi.org/10.1021/acsami.4c15939.

[22] Y. Yan, J. Wang, W. Wang, C. Han, Fine-tuning polyamide membrane pores and charge for enhanced Li+/Mg2+ separation, J. Memb. Sci. 721 (2025). https://doi.org/10.1016/j.memsci.2025.123812.

[23] S. Duan, S. Jiang, P. Xu, Z. Li, P. Zhang, Y. Liu, A. Matsuoka, Y. Lin, J. Shen, K. Guan, T. Yoshioka, H. Matsuyama, Boosting Nanofiltration Membrane Selectivity via Amine-Polymer Additive Engineering for Efficient Lithium Extraction From Brine, Advanced Science (2025). https://doi.org/10.1002/advs.202513172.

[24] E. Shi, Y. Liu, X. Wei, F. Zhao, T. Wang, Y. Du, C. Wang, C. Fan, Y. Yang, Y. Wang, Z. Jiang, Polyamide Nanofiltration Membrane through Aqueous Phase Additive-Mediated Interfacial Polymerization for Ion Separation, Ind. Eng. Chem. Res. (2026). https://doi.org/10.1021/acs.iecr.5c03745.

[25] Z. Si, Z. Zhang, C. Yin, T. Ju, M. Wei, J. Huang, Y. Wang, Engineering transport highways in microporous membranes for lithium extraction: The double role of covalent organic frameworks, J. Memb. Sci. 680 (2023). https://doi.org/10.1016/j.memsci.2023.121759.

[26] Y. Yan, J. Wang, W. Wang, C. Han, K. Huo, Q. Zhang, N. Wang, Efficient Li+/Mg2+ separation nanofiltration membranes modified by amine-functionalized TiO2 nanoparticles, J. Environ. Chem. Eng. 12 (2024). https://doi.org/10.1016/j.jece.2024.113627.

[27] P. Xu, J. Hong, Z. Xu, H. Xia, Q.Q. Ni, Novel aminated graphene quantum dots (GQDs-NH2)-engineered nanofiltration membrane with high Mg2+/Li+ separation efficiency, Sep. Purif. Technol. 258 (2021). https://doi.org/10.1016/j.seppur.2020.118042.

[28] Z. Wang, Z. Yang, X. Shi, Q. Zhang, W. Ma, Q. Bi, Y. Lin, Enhancement of Mg2+/Li+ selectivity and water permeability in nanofiltration membranes using dopamine-functionalized graphitic carbon nitride, J. Memb. Sci. 731 (2025). https://doi.org/10.1016/j.memsci.2025.124247.

[29] R. Jia, L.K. Wu, Z.L. Xu, M. Hedar, L.H. Luo, Y.Z. Wu, H.X. Li, Y.H. Tong, S.J. Xu, Efficient separation of Li+/Mg2+ via positively charged TFN membrane based on the PEI interlayer, Chem. Eng. Sci. 284 (2024). https://doi.org/10.1016/j.ces.2023.119523.

[30] Y. Liu, L. Gao, S. Li, L. Zhang, S. Yin, Tailoring MOF nanoparticle size in thin-film nanocomposite (TFN) membrane selective layers for enhanced Mg2+/Li+ selectivity, Desalination 615 (2025). https://doi.org/10.1016/j.desal.2025.119264.

[31] A. Aghaei, M. Amirul Islam, V. Rad, A. Khalili, A. Yousefi, A.A. Shamsabadi, M. Soroush, J.-Y. Cho, Y.-H. La, M. Sadrzadeh, Harvesting lithium from brines via high-selectivity nanofiltration integrated with membrane distillation, Chemical Engineering Journal 528 (2026) 172766. https://doi.org/10.1016/j.cej.2026.172766.

[32] M. Yassari, S.F. Seyedpour, B. Setegne, A. Aghaei, B. Ahvazi, M.D. Firouzjaei, M. Elliott, M. Sadrzadeh, Bioinspired Polypeptide Dendrimer-Modified Thin-Film Composite Membranes for Selective Lithium-Magnesium Separation with DFT Insights, Adv. Funct. Mater. 36 (2026) e27985. https://doi.org/10.1002/adfm.202527985.

[33] U. Noor, M.F. Farid, A. Sharif, A. Saleem, Z. Nabi, M.F. Mughal, K. Abbas, T. Ahmed, Functionalized carbon 1D/2D nanomaterials for effective water desalination: Synthesis, applications and cost issues. An overview, Desalination 571 (2024). https://doi.org/10.1016/j.desal.2023.117086.

[34] Z. Zhou, X. Zhu, Y. Yuan, S. Wang, X. Meng, T. Huhe, Q. Wang, A facile method to fabricate anti-fouling nanofiltration membrane with aminated lignin, J. Memb. Sci. 692 (2024). https://doi.org/10.1016/j.memsci.2023.122269.

[35] A. Taghipour, P. Karami, A. Khalili, M. Bagheri Kaloo, B. Ahvazi, A. Ullah, J.Y. Cho, M. Sadrzadeh, Lignin depolymerization: A sustainable strategy to enhance the separation performance of biopolymeric polyester membranes, J. Memb. Sci. 734 (2025). https://doi.org/10.1016/j.memsci.2025.124512.

[36] Y. Zhao, X. Shan, Q. An, Z. Xiao, S. Zhai, Interfacial integration of zirconium components with amino-modified lignin for selective and efficient phosphate capture, Chemical Engineering Journal 398 (2020). https://doi.org/10.1016/j.cej.2020.125561.

[37] H. Sun, G. Wang, J. Ge, N. Wei, W. Sui, Z. Chen, H. Jia, A.M. Parvez, C. Si, Reduction of lignin heterogeneity for improved catalytic performance of lignin nanosphere supported Pd nanoparticles, Ind. Crops Prod. 180 (2022). https://doi.org/10.1016/j.indcrop.2022.114685.

[38] R. Liu, A. Smeds, L. Wang, A. Pranovich, J. Hemming, S. Willför, H. Zhang, C. Xu, Fractionation of Lignin with Decreased Heterogeneity: Based on a Detailed Characteristics Study of Sequentially Extracted Softwood Kraft Lignin, ACS Sustain. Chem. Eng. 9 (2021). https://doi.org/10.1021/acssuschemeng.1c04725.

[39] A. Taghipour, P. Karami, A. Khalili, E. Jashni, B. Ahvazi, A. Ullah, J.-Y. Cho, M. Sadrzadeh, pH-Fractionated lignin enables high-selectivity, chlorine-tolerant polyester thin-film composite nanofiltration membranes, Chemical Engineering Journal 534 (2026) 175224. https://doi.org/10.1016/j.cej.2026.175224.

[40] Q. Li, Z. He, X. Yu, Q. Li, N. Zhang, Q. Zhang, C. Sun, Y. Liu, H. Deng, Lignin/polyamide composite nanofiltration membrane with ultra-high permeability for mono-/divalent salt separation, J. Memb. Sci. 719 (2025). https://doi.org/10.1016/j.memsci.2025.123751.

[41] W. Zhang, S. Zhao, H. Li, C. Lai, S. Zhang, W. Wen, C.Y. Tang, F. Meng, Lignin alkali regulated interfacial polymerization towards ultra-selective and highly permeable nanofiltration membrane, Nature Communications 16 (2025). https://doi.org/10.1038/s41467-024-55595-y.

[42] W. Sun, N. Zhang, Q. Li, X. Li, S. Chen, L. Zong, Y. Baikeli, E. Lv, H. Deng, X. Zhang, H. Baqiah, Bioinspired lignin-based loose nanofiltration membrane with excellent acid, fouling, and chlorine resistances toward dye/salt separation, J. Memb. Sci. 670 (2023). https://doi.org/10.1016/j.memsci.2023.121372.

[43] H. Pan, G. Sun, T. Zhao, Synthesis and characterization of aminated lignin, Int. J. Biol. Macromol. 59 (2013). https://doi.org/10.1016/j.ijbiomac.2013.04.049.

[44] A. Aghaei, A. Rahimpour, M. Sadrzadeh, Tailored L-Arginine modified Poly(piperazine-amide) nanofiltration membrane with enhanced water permeability for efficient Li+/Mg2+ separation, J. Memb. Sci. 728 (2025). https://doi.org/10.1016/j.memsci.2025.124140.

[45] R. Santiago, F.H. Bordón Sosa, I. Díaz, M. González-Miquel, J.A. Pereira Coutinho, Prediction of partition coefficients in aqueous organic systems using COSMO-RS, Sep. Purif. Technol. 379 (2025). https://doi.org/10.1016/j.seppur.2025.134942.

[46] S. Pronk, S. Páll, R. Schulz, P. Larsson, P. Bjelkmar, R. Apostolov, M.R. Shirts, J.C. Smith, P.M. Kasson, D. Van Der Spoel, B. Hess, E. Lindahl, GROMACS 4.5: A high-throughput and highly parallel open source molecular simulation toolkit, Bioinformatics 29 (2013). https://doi.org/10.1093/bioinformatics/btt055.

[47] J. Lee, X. Cheng, J.M. Swails, M.S. Yeom, P.K. Eastman, J.A. Lemkul, S. Wei, J. Buckner, J.C. Jeong, Y. Qi, S. Jo, V.S. Pande, D.A. Case, C.L. Brooks, A.D. MacKerell, J.B. Klauda, W. Im, CHARMM-GUI Input Generator for NAMD, GROMACS, AMBER, OpenMM, and CHARMM/OpenMM Simulations Using the CHARMM36 Additive Force Field, J. Chem. Theory Comput. 12 (2016). https://doi.org/10.1021/acs.jctc.5b00935.

[48] L. Martinez, R. Andrade, E.G. Birgin, J.M. Martínez, PACKMOL: A package for building initial configurations for molecular dynamics simulations, J. Comput. Chem. 30 (2009). https://doi.org/10.1002/jcc.21224.

[49] B. Hess, H. Bekker, H.J.C. Berendsen, J.G.E.M. Fraaije, LINCS: A Linear Constraint Solver for molecular simulations, J. Comput. Chem. 18 (1997). https://doi.org/10.1002/(SICI)1096-987X(199709)18:12<1463::AID-JCC4>3.0.CO;2-H.

[50] G. Bussi, D. Donadio, M. Parrinello, Canonical sampling through velocity rescaling, Journal of Chemical Physics 126 (2007). https://doi.org/10.1063/1.2408420.

[51] S. Kumar, J.M. Rosenberg, D. Bouzida, R.H. Swendsen, P.A. Kollman, THE weighted histogram analysis method for free-energy calculations on biomolecules. I. The method, J. Comput. Chem. 13 (1992). https://doi.org/10.1002/jcc.540130812.

[52] G. Hummer, Position-dependent diffusion coefficients and free energies from Bayesian analysis of equilibrium and replica molecular dynamics simulations, New J. Phys. 7 (2005). https://doi.org/10.1088/1367-2630/7/1/034.

[53] X. Meng, C. Crestini, H. Ben, N. Hao, Y. Pu, A.J. Ragauskas, D.S. Argyropoulos, Determination of hydroxyl groups in biorefinery resources via quantitative 31P NMR spectroscopy, Nat. Protoc. 14 (2019). https://doi.org/10.1038/s41596-019-0191-1.

[54] L. Liang, M. Peng, H. Xu, Z. Wu, B. Liu, C. Qin, C. Liang, C. Huang, S. Yao, Aminated lignin-modified polyethersulfone membranes with enhanced antifouling performance for oil-water separation, J. Environ. Chem. Eng. 13 (2025). https://doi.org/10.1016/j.jece.2025.119987.

[55] J.S. Mun, M.S. Khil, S.P. Mun, Preparation of aminated hardwood kraft lignin by Mannich reaction and its structural and thermal characterization, Journal of Wood Chemistry and Technology 45 (2025). https://doi.org/10.1080/02773813.2024.2446200.

[56] P. Karami, B. Khorshidi, L. Shamaei, E. Beaulieu, J.B.P. Soares, M. Sadrzadeh, Nanodiamond-Enabled Thin-Film Nanocomposite Polyamide Membranes for High-Temperature Water Treatment, ACS Appl. Mater. Interfaces 12 (2020). https://doi.org/10.1021/acsami.0c15194.

[57] P. Karami, B. Khorshidi, J.B.P. Soares, M. Sadrzadeh, Fabrication of Highly Permeable and Thermally Stable Reverse Osmosis Thin Film Composite Polyamide Membranes, ACS Appl. Mater. Interfaces 12 (2020). https://doi.org/10.1021/acsami.9b16875.

[58] P. Sarkar, S. Modak, S. Ray, V. Adupa, K.A. Reddy, S. Karan, Fast water transport through sub-5 nm polyamide nanofilms: The new upper-bound of the permeance-selectivity trade-off in nanofiltration, J. Mater. Chem. A Mater. 9 (2021). https://doi.org/10.1039/d1ta04763a.

[59] E. Jashni, A. Aghaei, M. Amirul Islam, A. Taghipour, F. Rezaie, A. Khalili, J.Y. Cho, M. Sadrzadeh, Polyamide thin film nanocomposite membranes modified with cationic nanogel for efficient Li+/Mg2+ separation, Desalination 616 (2025). https://doi.org/10.1016/j.desal.2025.119336.

[60] B. Tansel, Significance of thermodynamic and physical characteristics on permeation of ions during membrane separation: Hydrated radius, hydration free energy and viscous effects, Sep. Purif. Technol. 86 (2012). https://doi.org/10.1016/j.seppur.2011.10.033.

[61] A. Taghipour, M. Dadashi Firouzjaei, C. Ammann, M. Elliott, P. Karami, A. Rahimpour, M. Sadrzadeh, Unveiling the impact of monomer reactivity on the morphology and functionality of thin-film composite membranes, Chemical Engineering Journal 480 (2024). https://doi.org/10.1016/j.cej.2023.148028.

[62] X. Liu, Y. Feng, Y. Ni, H. Peng, S. Li, Q. Zhao, High-permeance Mg2+/Li+ separation nanofiltration membranes intensified by quadruple imidazolium salts, J. Memb. Sci. 667 (2023). https://doi.org/10.1016/j.memsci.2022.121178.

[63] S. Xu, J. Song, Q. Bi, Q. Chen, W.M. Zhang, Z. Qian, L. Zhang, S. Xu, N. Tang, T. He, Extraction of lithium from Chinese salt-lake brines by membranes: Design and practice, J. Memb. Sci. 635 (2021). https://doi.org/10.1016/j.memsci.2021.119441.

[64] H. Li, Y. Wang, T. Li, X.K. Ren, J. Wang, Z. Wang, S. Zhao, Nanofiltration membrane with crown ether as exclusive Li+ transport channels achieving efficient extraction of lithium from salt lake brine, Chemical Engineering Journal 438 (2022). https://doi.org/10.1016/j.cej.2022.135658.

[65] P. Xu, J. Hong, X. Qian, Z. Xu, H. Xia, Q.Q. Ni, "Bridge" graphene oxide modified positive charged nanofiltration thin membrane with high efficiency for Mg2+/Li+ separation, Desalination 488 (2020). https://doi.org/10.1016/j.desal.2020.114522.

[66] T. Li, X. Zhang, Y. Zhang, J. Wang, Z. Wang, S. Zhao, Nanofiltration membrane comprising structural regulator Cyclen for efficient Li+/Mg2+ separation, Desalination 556 (2023). https://doi.org/10.1016/j.desal.2023.116575.

[67] W. Wang, J. Wang, Y. Yan, K. Huo, C. Han, Q. Zhang, Structure and positive charge regulation in nanofiltration membrane by novel nanomaterial g-C3N5 for efficient Li+/Mg2+ separation, J. Memb. Sci. 707 (2024) 122984. https://doi.org/10.1016/J.MEMSCI.2024.122984.

[68] N. Yang, K. Li, Y. Hao, L. Zhang, Y. Sun, L. Zhang, B. Jiang, Advanced Mg2+/Li+ separation nanofiltration membranes fabricated with Girard's reagent T based on functional end-capping strategy, J. Memb. Sci. 695 (2024). https://doi.org/10.1016/j.memsci.2024.122483.

[69] Y. Yin, C. Li, D.Y.F. Ng, R. Wang, Quaternary ammonium-regulated fabrication of hollow fiber nanofiltration membrane for enhanced Mg2+/Li+ separation, J. Memb. Sci. 726 (2025). https://doi.org/10.1016/j.memsci.2025.124064.

[70] X. Yi, S.-L. Li, J. Xiao, N. Ullah, H. Zuo, Y. Hu, G. Gong, Positively charged polyamide nanofiltration membrane via grafting a bis-pyridinium molecule for high-efficiency Mg2+/Li+ separation, J. Memb. Sci. 743 (2026). https://doi.org/10.1016/j.memsci.2026.125182.

[71] B. Zhao, M. Pei, X. Guo, Y. Zhang, L. Wang, Z. Zhang, Enhanced Mg2+/Li+ separation by Janus nanofiltration membrane incorporated with negatively-charged COF interlayer, Sep. Purif. Technol. 365 (2025). https://doi.org/10.1016/j.seppur.2025.132671.

[72] K. Li, Y. Hao, N. Yang, L. Zhang, L. Zhang, Y. Sun, B. Jiang, Capping-grafting synergistic strategy for the preparation of high-performance Mg2+/Li+ separation nanofiltration membranes, J. Memb. Sci. 713 (2025) 123311. https://doi.org/10.1016/J.MEMSCI.2024.123311.

Journal Pre-proof

Declaration of interests

The authors declare that they have no known competing financial interests or personal relationships that could have appeared to influence the work reported in this paper.

Highlights

- Aminated lignin regulates interfacial polymerization during the synthesis of NF membranes.
- COSMO-RS and MD reveal thermodynamic and kinetic modulation of monomer transport.
- The optimized membrane achieves a Li^+/Mg^{2+} selectivity of 51.2 in simulated brine.
- Lignin incorporation enhances Mg^{2+} rejection while maintaining high water flux.
- Bio-based lignin additive enables sustainable lithium-selective nanofiltration membranes.

Journal Pre-proof